

# Modelling narrow-line regions of active galaxies in the Sloan Digital Sky Survey - I. Sample selection and physical conditions

Zhitai Zhang<sup>1,2\*</sup>, Yanchun Liang<sup>1</sup> and François Hammer<sup>3</sup>

<sup>1</sup>Key Laboratory of Optical Astronomy, National Astronomical Observatories, CAS, 20A Datun Road, 100012 Beijing, PR China

<sup>2</sup>University of Chinese Academy of Sciences, 19A Yuquan Road, Shijingshan District, 100049, Beijing, China

<sup>3</sup>GEPI, Observatoire de Paris, CNRS, University Paris Diderot, 5 place Jules Janssen, 92195 Meudon, France

Accepted 2012 December 24. Received 2012 December 24; in original form 2012 April 17

## ABSTRACT

Using spectroscopy from the Sloan Digital Sky Survey Data Release Seven, we systematically determine the electron density  $n_e$  and electron temperature  $T_e$  of active galaxies and star-forming galaxies while mainly focusing on the narrow-line regions (NLRs). Herein active galaxies refer to composites, low-ionization narrow emission-line regions (LINERs) and Seyferts following the Baldwin-Phillips-Terlevich diagram classifications afforded by the SDSS data. The plasma diagnostics of  $n_e$  and  $T_e$  are determined through the  $I[\text{S II}] \lambda 6716/\lambda 6731$  and  $I[\text{O III}] \lambda 5007/\lambda 4363$  ratios, respectively. By simultaneously determining  $n_e$  from  $[\text{S II}]$  and  $T_e$  from  $[\text{O III}]$  in our  $[\text{O III}] \lambda 4363$  emission sample of 15 019 galaxies, we find two clear sequences:  $T_{\text{LINER}} \gtrsim T_{\text{composite}} > T_{\text{Seyfert}} > T_{\text{star-forming}}$  and  $n_{\text{LINER}} \gtrsim n_{\text{Seyfert}} > n_{\text{composite}} > n_{\text{star-forming}}$ . The typical range of  $n_e$  in the NLRs of active galactic nuclei (AGNs) is  $10^{2-3} \text{ cm}^{-3}$ . The temperatures in the NLRs range from 1.0 to  $2.0 \times 10^4$  K for Seyferts, and the ranges were even higher and wider for LINERs and composites. The transitions of  $n_e$  and  $T_e$  from the NLRs to the discs are revealed.

We also present a comparative study, including stellar mass ( $M_*$ ), specific star formation rate ( $\text{SFR}/M_*$ ) and plasma diagnostic results. We propose that  $Y_L \gtrsim Y_{SY} > Y_C > Y_{SF}$ , where  $Y$  is the characteristic present-day star-formation time-scale. One remarkable feature of the Seyferts shown on an  $M_*$ - $\text{SFR}/M_*$  diagram, which we call the evolutionary pattern of AGN with high ionization potential, is that the strong  $[\text{O III}] \lambda 4363$  Seyferts distribute uniformly with the weak Seyferts, definitely a reverse of the situation for star-forming galaxies. It is a natural and well-known consensus that strong  $[\text{O III}] \lambda 4363$  emissions in star-forming galaxies imply young stellar populations and thus low stellar masses. However, in the AGN case, several strong lines of evidence suggest that some supplementary energy source(s) should be responsible for high ionization potential.

**Key words:** surveys – galaxies: active – galaxies: ISM – galaxies: Seyfert – galaxies: statistics

## 1 INTRODUCTION

The investigation of the narrow-line regions (NLRs) of active galactic nuclei (AGN) is important for a number of reasons. The NLR provides a bridge from the familiar and relatively well understood to the exotic and poorly known. On one hand, this region connects on its inner side with the more compact emitting regions that are spatially unresolved (except in the radio) and occur in very obscure surroundings. On the other hand, the outer boundary of the NLR does not just conjoin with the interstellar medium (ISM) of the galaxy but it can often be well spatially resolved at optical wavelengths. Ferland & Netzer (1983) were the first to attempt to model the NLRs of AGNs, and many other studies followed. Emission-line region models are used to determine

the physical conditions of the ionized gas (for details, refer to Dopita & Sutherland 2003). Currently, two main ionization sources are most frequently applied: photoionization and shock ionization (refer to an overview of modelling NLRs in Groves 2007). In addition to the ionization status, the geometry, spatial extent and emission from this region could also be explained and reproduced by modelling the NLRs. However, before running the models, it should be noted that all of these types of models rely on pre-estimates of some input parameters (e.g. density and temperature). Fortunately, the emission lines observed in the NLRs of AGNs are much the same as those observed in H II regions and planetary nebulae. Therefore, the standard nebular diagnostic methods can be applied to determine the electron density and temperature in the NLRs of AGNs (see Osterbrock & Ferland 2006 for more details). One of the earliest and most well-studied examples is the NLR in Cyg A. The amount of extinction calculated from the Balmer decre-

\* E-mail: ztzhang@nao.cas.cn

ment giving the best overall fit with the recombination decrement for  $T_e=10^4$  K,  $n_e=10^4$  cm $^{-3}$  in Cyg A (Osterbrock & Miller 1975; Osterbrock 1983). Koski (1978) have found that the average density in the line-emitting gas of 20 Seyfert 2 galaxies is approximately 2000 cm $^{-3}$  and that the average temperature is approximately 12 000 ~ 25 000 K. Walsh (1983) has studied the Seyfert nuclei of NGC 1068 and has found that the electron density range is  $9 \times 10^4$  to  $5 \times 10^5$  cm $^{-3}$ , assuming an electron temperature of  $\sim 15$  000 K.

Two different types of strategies are often applied to investigate an object class: one is to study one or a few well-observed individual objects, and the other is to study a large sample of objects. The advantage of the former strategy is the more detailed and accurate treatment of data, yet it poses the risk of misidentifying the truly representative characteristics. In contrast, the latter strategy, which is usually based on a homogeneous data-set, allows us to utilize the information contained in collective trends and correlations. The former strategy has been more frequently used when investigating the physical conditions of NLRs (e.g. Kraemer, Ruiz & Crenshaw 1998; Kalsner et al. 2000; Barth et al. 2001; Collins et al. 2009; Kraemer et al. 2009). In comparison, there have been only a few previous estimates of the density and temperature of a large sample of AGN NLRs (e.g. Rodríguez et al. 2000; Sulentic, Marziani & Dultzin-Hacyan 2000; Bennert et al. 2006; Xu et al. 2007). Because of the success of the Sloan Digital Sky Survey (SDSS), we have a large data set to use in order to investigate the NLRs of AGNs in the local Universe (e.g. Hao et al. 2005a,b; Zhou et al. 2006; Liu et al. 2010; Shen et al. 2011). In order to prepare accurate and trustworthy input parameters for the next-step modelling, we follow the second strategy in this study.

Narrow emission-line galaxies can be generally separated into four classes: star-forming galaxies, composites, low-ionization nuclear emission-line region (LINERs), and Seyfert galaxies. It is important to understand how these four classes differ in their ionization sources and thus temperatures, densities as well as emission, in order to build a picture of the local Universe. Baldwin, Phillips & Terlevich (1981) (hereafter BPT) have proposed using optical emission-line ratios to classify the dominant energy source in emission-line galaxies. The BPT diagrams are sensitive to the hardness of the ionizing radiation field. The first semi-empirical classification to be used with the standard optical diagnostic diagrams was derived by Osterbrock & de Robertis 1985 and Veilleux & Osterbrock 1987, providing better optical classifications. These classification schemes have been significantly improved using the SDSS (e.g. Kewley et al. 2006, hereafter Ke06). With the improved optical classifications, for the first time, we are able to analyse the plasma diagnostic results accurately and to systematically distinguish between the different classes within an observationally homogeneous sample.

The present paper is organised as follows. In Section 2, we give a description of our sample selection criteria. Sample definitions are included in Section 3, while Section 4 is devoted to the plasma diagnostic results. In Section 5, we focus on NLRs, providing statistical  $n_e$  and  $T_e$  analyses and making comparisons between different classes. In Section 6, we further apply the diagnostic results obtained and present a comparative study dealing with the relationships of physical properties, such as stellar mass ( $M_\star$ ) and specific star formation rate (SFR/ $M_\star$ ), in different classes. In Section 7, we discuss the shock effects and low-metallicity AGN candidates for further study. Finally, we summarize our main results in Section 8. Throughout this paper, we assume a flat  $\Lambda$ CDM cosmology with  $\Omega_m = 0.3$ ,  $\Omega_\Lambda = 0.7$ , and  $H_0 = 70$  km s $^{-1}$  Mpc $^{-1}$ .

## 2 SAMPLE SELECTION

The SDSS (York et al. 2000; Stoughton et al. 2002) uses a dedicated, wide-field, 2.5-m telescope (Abazajian et al. 2009) at the Apache Point observatory, New Mexico, for CCD imaging in five broad-bands, *ugriz*, over 10 000 deg $^2$  of high-latitude sky, and for the spectroscopy of a million galaxies and 100 000 quasars over this same region; these goals have been realized with the seventh public data release (DR7 $^1$ ; Abazajian et al. 2009). The images were reduced (Lupton et al. 2001; Stoughton et al. 2002; Pier et al. 2003; Ivezić et al. 2004) and calibrated (Hogg et al. 2001; Smith et al. 2002; Tucker et al. 2006), and galaxies were selected in two ways for follow-up spectroscopy covering 3800-9200 Å at a resolution of  $\lambda/\Delta\lambda \simeq 1800$ . The spectra were taken using 3-arcsec diameter fibres, positioned as close as possible to the centres of the target galaxies. Several improvements have been made to the spectroscopic software since DR5, particularly with regards to wavelength calibration, spectrophotometric calibration and the handling of strong emission lines (Adelman-McCarthy et al. 2008; Abazajian et al. 2009).

The SDSS data base has been explored by several groups, using different approaches and techniques. Our analysis is based on data products from the catalogues $^2$  obtained by the Max-Planck Institute for Astronomy (MPA, Garching) and John Hopkins University (JHU). The MPA/JHU catalogues are excellent resources for statistical studies of nearby narrow-line AGN populations because of the very large sample size (e.g. 33 589 AGN in DR2 and 88 178 in the DR4 catalogue) and because of the inclusion of additional data for the host galaxies, such as emission-line analyses and some derived physical properties, including stellar masses (Kauffmann et al. 2003a; Gallazzi et al. 2005; Salim et al. 2007), star formation rates (Brinchmann et al. 2004), and gas phase metallicities for star-forming galaxies (Tremonti et al. 2004). The MPA/JHU group has publicly released catalogues for a total of 927 552 SDSS galaxies corresponding to DR7, a significant increase in size from their previous DR4 release. A number of improvements are made due to developments both in the SDSS reduction and analysis pipelines. The emission-line fluxes given in the MPA/JHU catalogues have all been corrected for foreground (galactic) reddening (O'Donnell 1994).

### 2.1 Selection criteria

Our sample selection criteria are as follows.

(i) The signal-to-noise (S/N) is  $> 5$  in the strong emission lines [O II]  $\lambda 3726$ , 29 Å, H $\beta$   $\lambda 4861$  Å, [O III]  $\lambda 5007$  Å, [O I]  $\lambda 6300$  Å, H $\alpha$   $\lambda 6563$  Å, [N II]  $\lambda 6584$  Å, [S II]  $\lambda 6716$ , 31 Å. The S/N criteria are required so that we can accurately classify the galaxies into star-forming or AGN-dominated classes. As discussed on the website $^3$ , the uncertainties (i.e. \*\_FLUX\_ERR) are likely to be underestimates of the true uncertainties. By using the duplicate observations of galaxies to compare the empirical spread in value determinations with the random errors, the MPA/JHU group presents the results given as ‘scale uncertainties’ in their DR7 release to correct for the underestimates. We adopt this correction and increase the uncertainty estimates on the emission lines by multiplying by the listed line flux uncertainty estimate factors.

<sup>1</sup> <http://www.sdss.org/dr7>

<sup>2</sup> Available at <http://mpa-garching.mpg.de/SDSS/DR7>

<sup>3</sup> [http://www.mpa-garching.mpg.de/SDSS/DR7/raw\\_data.html](http://www.mpa-garching.mpg.de/SDSS/DR7/raw_data.html)

(ii) Objects with no stellar mass ( $M_*$ ) measurements (both total and fibre estimates) and poor specific star formation rate ( $\text{SFR}/M_*$ ) estimation (i.e.  $\text{FLAG} = 1$ ) in the catalogues are excluded. We utilize these two derived parameters to probe the galaxy formation histories of different classes of emission-line galaxies in our sample.

(iii) Broad-line AGN contaminations are removed. Hao et al. (2005a) have discussed the method of identifying broad-line AGNs in the SDSS DR4 spectra. They have proposed  $\text{FWHM}(H\alpha) > 1200 \text{ km s}^{-1}$  as the selection criterion for defining broad-line AGNs. We apply this classification to our data to remove broad-line AGN contaminations, using the  $\text{SIGMA\_BALMER}$  given in the MPA/JHU catalogues to derive  $\text{FWHM}_{\text{Balmer}} = \text{SIGMA\_BALMER} \times 2.355$ .

Note that herein we have not included any cuts on redshift, as in previous works on SDSS emission-line galaxies (e.g. Ke06). In fact, the aperture effects, in Section 5, we present and discuss the aperture effects, or more precisely how the determined  $n_e$  and  $T_e$  (plasma diagnostics in Section 4) vary as a function of the physical aperture size. Although LINERs typically have lower luminosities than Seyfert galaxies and are therefore found at lower redshifts than Seyferts in the magnitude-limited SDSS, this issue does not strongly affect our analysis because we are only interested in the typical range and representative values of  $n_e$  and  $T_e$ .

After applying the above three criteria, our resulting parent sample contains 46 867 emission-line galaxies.

## 2.2 Extinction correction

The emission line fluxes are corrected for dust extinction. In this study, we use the assumptions given by previous studies. We use the Balmer decrement for Case B recombination at  $T = 10^4 \text{ K}$  and  $n_e \sim 10^{2-4} \text{ cm}^{-3}$ , the dust-free Balmer-line ratio  $H\alpha/H\beta$  value of 2.86 for star-forming galaxies and theoretical AGN value of 3.1 for composite galaxies, LINERs and Seyferts, and the relation given by Osterbrock & Ferland (2006)

$$\left(\frac{I_{H\alpha}}{I_{H\beta}}\right)_{\text{obs}} = \left(\frac{I_{H\alpha 0}}{I_{H\beta 0}}\right)_{\text{intr}} 10^{-c(f(H\alpha)-f(H\beta))}. \quad (1)$$

Applying the average interstellar extinction law, we have  $f(H\alpha) - f(H\beta) = 0.347$  as summarized from Fitzpatrick (1999).

Theoretically, the Balmer decrement has been determined over a range of temperatures and densities for two cases: Case A (assuming the Lyman series is optically thin) and Case B (assuming the Lyman series is optically thick). Generally, Case B recombination is a better approximation for most nebulae. Some calculated Case B results (i.e. ratio descriptions) for the H I recombination lines have been given by table B.7 in Dopita & Sutherland (2003) or table 4.4 in Osterbrock & Ferland (2006). Although we can conversely obtain observational Balmer decrements with Balmer series measurements using  $n_e$  and  $T_e$  estimates and the given ratio descriptions, the variations as a result of temperature and density should not be significant compared with our current values. Furthermore, although we can predict the  $H\alpha/H\beta$  value for Case B by using the  $T_e$  and  $n_e$  estimates, considerable errors must be introduced by not only the measurements of line intensity uncertainties but also the algorithm used for solving  $n_e$  and  $T_e$ . We should mention here that Groves, Brinchmann & Walcher (2012) have found a systematic bias in the SDSS DR7 MPA/JPU catalogues (i.e. a 0.35-Å underestimation of the emission-line  $H\beta$  equivalent width) and have suggested that the DR7  $A_V$  estimates could be overestimated by a mean difference of -0.07 mag. However, this effect is not important in our analysis.

**Table 1.** Sample divisions based on [O III]  $\lambda 4363$  detection quality. Fluxes summarized here are pre-extinction correction measurements of the [O III]  $\lambda 4363$  line (in units of  $10^{-17} \text{ erg s}^{-1} \text{ cm}^{-2}$ ). Luminosities listed are in units of  $L_\odot$  after extinction correction. Note that  $L_{[\text{O III}]}$  is the luminosity of [O III]  $\lambda 5007$ .

	Sample A	Sample B	Sample C
Number	1098	1409	13 210
S/N	>5	3-5	1-3
$z_{\text{median}}$	0.070	0.067	0.075
$z_{\text{range}}$	0.03-0.32	0.02-0.29	0.02-0.32
$\text{Flux}_{\text{median}}$	31.0	13.3	5.0
$\text{Flux}_{\text{range}}$	6.2-480.9	4.9-66.1	1.1-50.1
$\log L_{[\text{O III}]}$	8.32	8.01	7.47
$\log L_{H\beta}$	7.59	7.45	7.47

## 3 SAMPLE DEFINITION

### 3.1 Sample: [O III] $\lambda 4363$ detection quality

Precise  $T_e$  measurements require careful CCD calibrations, along with fairly high-quality spectra. In practice, however, the [O III]  $\lambda 5007/\lambda 4363$  ratio is quite large and is thus difficult to measure accurately. Therefore, we further reject 31 150 objects with poor [O III]  $\lambda 4363$  detection quality (i.e.  $\text{S/N} < 1$ ). The remaining 15 717 objects are divided into the three samples shown in Table 1: strong (sample A), intermediate (sample B), and weak (sample C) [O III]  $\lambda 4363$  emission samples, respectively. As expected, we see that stronger [O III]  $\lambda 4363$  objects display significantly higher luminosities of [O III]  $\lambda 5007$  ( $L_{[\text{O III}]}$ ).

The three most widely used BPT diagrams are applied to classify the emission-line galaxies: [N II]  $\lambda 6584/H\alpha$  versus [O III]  $\lambda 5007/H\beta$  (hereafter [N II]/ $H\alpha$  versus [O III]/ $H\beta$ ), [S II]  $\lambda 6584/H\alpha$  versus [O III]  $\lambda 5007/H\beta$  (hereafter [S II]/ $H\alpha$  versus [O III]/ $H\beta$ ) and [O I]  $\lambda 6584/H\alpha$  versus [O III]  $\lambda 5007/H\beta$  (hereafter [O I]/ $H\alpha$  versus [O III]/ $H\beta$ ) (e.g. Veilleux & Osterbrock 1987). Using the calibrations obtained by Kewley et al. (2001) (hereafter Ke01), Kauffmann et al. (2003c) (hereafter Ka03) and Ke06, we subdivide each of the three samples into four classes: star-forming galaxies, composites, LINERs, and Seyferts.

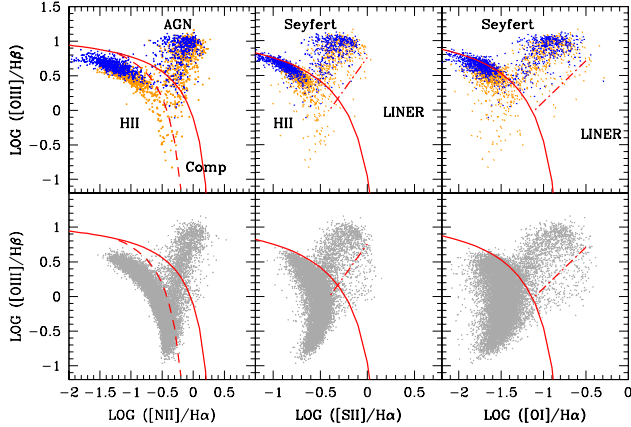
According to this scheme, our sample of 15 717 galaxies contains 1842 (11.7 per cent) Seyferts, 95 (0.6 per cent) LINERs, 1338 (8.5 per cent) composites, and 11 744 (74.7 per cent) star-forming galaxies. The rest are ambiguous galaxies (698; 4.4 per cent), which are classified as one type of object in one or two diagrams and classified as another type of object in the remaining diagram(s). Hereafter we exclude the 698 ambiguous galaxies. Fig. 1 shows the sample distributions in the three BPT diagrams. It is confirmed that (strong) [O III]  $\lambda 4363$  is more easily detected for Seyferts, which is also a clue for some alternative source of ionization in these galaxies. The compositions of the different galaxy classes in sample A, B and C are shown in Table. 2. It is clear that  $L_{[\text{O III}]}$  shows a correlation with the [O III]  $\lambda 4363$  intensity, an effect that is not seen in  $L_{H\beta}$ . Seyferts, LINERs and composites have similar redshift values, and are more distant than star-forming galaxies (refer to Table. 2). In addition, Seyferts and LINERs have higher  $L_{[\text{O III}]}$  than composites and star-forming galaxies, which suggests different ionization sources are present in different type of galaxies.

After performing extinction corrections, we calculate  $A_V$  in seven  $M_*$  bins (see Table. 3), where  $A_V = R_V \times E(B - V) = (3.1c)/1.47$  where  $R_V = 3.1$ , on average, in the Milky Way and



**Table 3.** Summary of  $A_V$  in seven  $M_\star$  bins. The superscripts show the sample size of those samples that have a sample size no larger than 10.

log $M_\star$ ( $M_\odot$ )	Seyferts			LINERs			Composites			Star-forming galaxies		
	A	B	C	A	B	C	A	B	C	A	B	C
8.1			0.29 <sup>1</sup>							0.25	0.28	0.39
8.7							0.05 <sup>2</sup>		0.53 <sup>3</sup>	0.29	0.32	0.33
9.3	0.24 <sup>7</sup>	0.42 <sup>3</sup>	0.35 <sup>3</sup>				0.31 <sup>5</sup>	0.24 <sup>4</sup>	0.37 <sup>8</sup>	0.32	0.40	0.45
9.8	0.56	0.72	0.47			1.09 <sup>5</sup>	0.57 <sup>3</sup>	0.53	0.60	0.46	0.55	0.68
10.3	0.63	0.62	0.74			1.17	0.57	0.67	0.82	0.68	0.90	1.01
10.7	0.63	0.84	0.84			1.19 <sup>3</sup>	0.96	0.81 <sup>10</sup>	0.89	1.11	1.08 <sup>10</sup>	1.36
11.2	0.72	0.86	0.96	0.35 <sup>1</sup>	0.95 <sup>2</sup>	1.10		1.30 <sup>3</sup>	1.35		0.46 <sup>1</sup>	1.59

**Figure 1.** Three BPT diagrams (from left to right): the  $[N\ II]/H\alpha$  versus  $[O\ III]/H\beta$  diagram, the  $[S\ II]/H\alpha$  versus  $[O\ III]/H\beta$  diagram and the  $[O\ I]/H\alpha$  versus  $[O\ III]/H\beta$  diagram. Top panels: sample A (blue, upper) and sample B (orange, lower) are illustrated. Bottom panels: sample C objects (grey) are presented. The Ke01 extreme starburst classification line (solid line), the Ka03 pure star formation line (dashed line) and the Ke06 Seyfert-LINER line (dot-dashed line) are used to separate galaxies into four classes: star-forming galaxies, composites, Seyferts and LINERs.**Table 2.** Number distribution of the subsamples discussed in the text, and a summary of the mean redshift and luminosity (in units of  $L_\odot$ ).

Subsample	Object	Number	Redshift	Luminosity	
				$\log L_{[O\ III]}$	$\log L_{H\beta}$
ASY	Seyfert	371	0.098	8.64	7.75
AL	LINER	1	0.053	7.66	7.25
AC	composite	33	0.107	8.35	7.85
ASF	star-forming	529	0.071	8.08	7.44
BSY	Seyfert	419	0.096	8.41	7.55
BL	LINER	5	0.107	8.46	8.01
BC	composite	82	0.099	8.07	7.78
BSF	star-forming	795	0.073	7.81	7.34
CSY	Seyfert	1052	0.100	8.24	7.52
CL	LINER	89	0.085	7.74	7.40
CC	composite	1223	0.094	7.79	7.83
CSF	star-forming	10 420	0.077	7.37	7.42

$E(B - V) = c/1.47$  for the standard Galactic extinction law (refer to equation 1 for  $c$ ; Osterbrock & Ferland 2006). The following two relations are revealed: comparisons between samples A, B and C show  $A_{V-A} < A_{V-B} < A_{V-C}$ ; comparisons between the four classes of emission-line galaxies show  $A_{V-Seyfert} < A_{V-Comp}$

$\lesssim A_{V-StarForming} \lesssim A_{V-LINER}$  at constant  $M_\star$ . The first relation could be explained by a selection bias because it is far more difficult to observe faint lines, such as  $[O\ III]\ \lambda 4363$ , in a heavily obscured medium. Considering the second relation, the sampled LINERs as a group have the highest  $A_V$ . Because of supernova remnants, the high  $A_V$  in LINERs most likely indicates the coexistence of old stellar populations and some specific high-energy process.

### 3.2 Class: NLR-dominated objects

The NLR is generally a few kiloparsecs across (e.g. Bennert et al. 2002; Netzer et al. 2004), although ionized gas has been seen at even larger ranges in some objects. Therefore, the NLR is a limited-small region in its host galaxy, and is most likely a combination of gas fluorescing in response to the active nuclei and material being ionized by massive stars nearby. The SDSS 3-arcsec diameter fibres subtend a variable amount of the total light as the redshift varies; therefore, the aperture effects are significant when considering physical conditions such as  $n_e$  and  $T_e$ . In this section, we focus on the NLRs in our samples to gain insight into the relative contributions of the NLR and disc as the physical aperture sizes vary.

In the spectra of Seyfert 2 galaxies, the narrow (permitted and forbidden) emission lines show typical linewidths (FWHM) of 300-500  $\text{km s}^{-1}$  (e.g. Kollatschny & Wang 2006). For LINERs, the FWHM (permitted and forbidden) could be even greater than those of the Seyfert 2 galaxies. Fig. 2 shows histograms of  $\text{FWHM}_{\text{Balmer}}$  for active galaxies (i.e. Seyferts, LINERs and composites; cf. the estimation of  $\text{FWHM}_{\text{Balmer}}$  in Section 2). The linewidths range from 100 to 600-800  $\text{km s}^{-1}$  with median values of 250, 335, and 419  $\text{km s}^{-1}$  for composites, Seyferts, and LINERs, respectively. We also check the FWHM of forbidden lines and the median values (in the same order) are: 264, 341 and 439  $\text{km s}^{-1}$ . Not surprisingly, the transition objects (i.e. composites) have narrower lines compared to LINERs, as is expected because of differences in their average Hubble types and the well-known dependence of nebular linewidth on bulge prominence (e.g. Ho 1996). In addition, we see that LINERs have wider permitted lines than Seyferts. Table 4 summarizes the FWHM-selected objects in detail. It is not surprising that objects with  $\text{FWHM}_{\text{Balmer}} > 300\ \text{km s}^{-1}$  are much more easily found in LINERs and Seyferts than in composites. Here, we notice that there are 168 (with  $S/N > 1$ ;  $\sim 1.4$  per cent) narrow-line star-forming galaxies. Thus we plot these star-forming galaxies in the BPT diagram (i.e.  $[N\ II]/H\alpha$  versus  $[O\ III]/H\beta$ ) and we find that these objects generally lie along the Ka03 pure star-forming line with no significant dispersions; we suppose they could be misclassified and actually be transition objects (i.e. composites).

Bennert et al. (2006) have studied the NLRs in Seyfert 2 galaxies from spatially resolved optical spectroscopy. They have

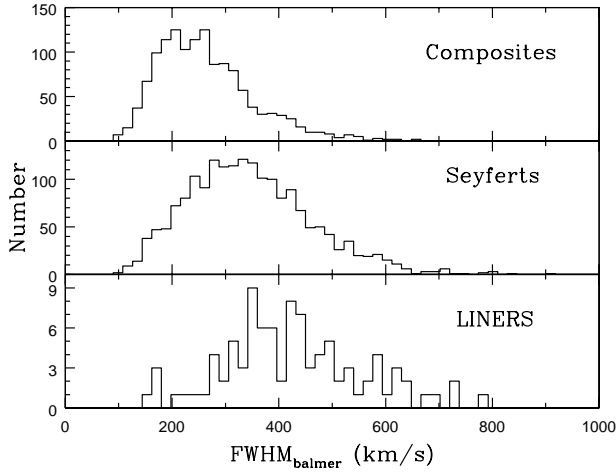


**Figure 2.** Histograms of FWHM of Balmer lines for the three types of emission-line galaxies (from top to bottom): composites, Seyferts and LINERs.

**Table 4.** Summary of objects with  $\text{FWHM}_{\text{Balmer}} > 300 \text{ km s}^{-1}$ .

Object	S/N > 1		S/N > 3	
	Number	Per cent	Number	Per cent
Seyfert(1842)	1141	61.9	540	29.3
LINER(95)	82	86.3	6	0.63
Composite(1338)	383	28.6	46	3.4
SF(11 744)	168	1.4	28	0.2

suggested that the lower limits of NLR size are 1-5 kpc and are limited by either the S/N data or the lack of a strong surrounding stellar ionization field. We convert redshifts into physical aperture size (i.e.  $\phi$  in kpc) for the SDSS 3-arcsec fibre. Ho (2008) has claimed that the NLRs in luminous Seyferts span from 50 pc to 1 kpc in radius. Additionally, Bennert et al. (2002) have measured the NLR sizes based on a sample of Seyferts. They have found a strong correlation between the NLR radius ( $R_{\text{NLR}}$ ) and the [O III]  $\lambda 5007$  luminosity, which was scaled to the cosmology by Netzer et al. (2004), adopted in this paper. This can be written as

$$R_{\text{NLR}} = 2.1 L_{[\text{O III}]\lambda 5007}^{0.52 \pm 0.06} \text{ (in kpc)}, \quad (2)$$

where  $L_{[\text{O III}]\lambda 5007}^{0.52 \pm 0.06} = L_{[\text{O III}]\lambda 5007} / 10^{42} \text{ erg s}^{-1}$  (the uncertainty on the constant 2.1 kpc is of the order of 15 per cent). We adopt this correlation to constrain the upper limits of  $R_{\text{NLR}}$  in order to compare with the sampled aperture size ( $R_{\text{obs}}$ ). Fig. 3 illustrates our NLR selection criteria. We require that  $\ln \phi < 1$  kpc,  $\text{FWHM}_{\text{Balmer}} > 300 \text{ km s}^{-1}$  and  $R_{\text{obs}} < R_{\text{NLR}}$  for the so-called NLR-dominated (hereafter ND) objects. The other two classes are the disc-contaminated NLR (hereafter DN) and non-NLR (hereafter NN) objects. Table 5 is a summary of the three classes of objects. We examine how  $n_e$  and  $T_e$  vary as velocity dispersion increases. The results agree with the suggestion given by Heckman et al. (1981) that the kinematics and physical conditions of the narrow-line emitting gas are not strongly coupled. We utilize the class definitions in Section 5.

#### 4 PLASMA DIAGNOSTIC RESULTS

The two best examples frequently used to measure the electron density are [S II]  $\lambda 6716$ , 31 and [O II]  $\lambda 3726$ , 29. However, the typical

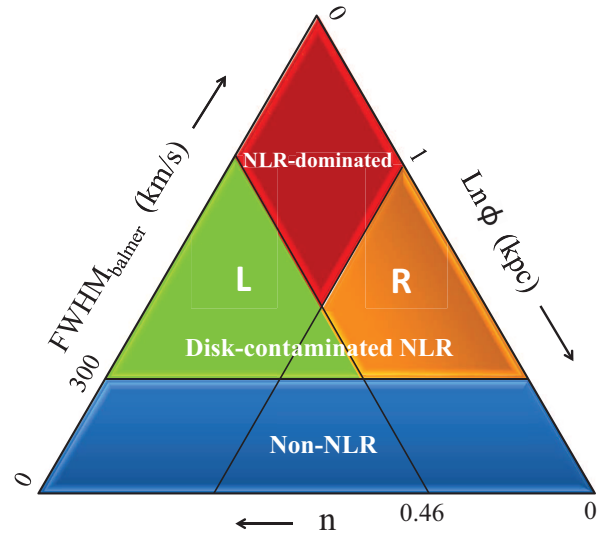


**Figure 3.** This ternary diagram illustrates selection criteria of the NLR-dominated objects (top red diamond). The disc-contaminated NLR objects occupy the left (L; green triangle) and right (R; orange trapezoidal) regions, while bottom blue trapezoid is occupied by the non-NLR objects. The arrows show scaling directions. Refer to equation (2) for the power law index  $n$ .

linewidths (FWHM) in NLRs, ranging from 300 to 500  $\text{km s}^{-1}$  (e.g. Kollatschny & Wang 2006), are comparable to, or are even larger than, the separation of the two [O II] lines, approximately 300  $\text{km s}^{-1}$ . Therefore, the [O II] intensity ratio, which is a good electron density diagnostic in H II regions and planetary nebulae, cannot be applied to AGNs (Osterbrock & Ferland 2006). The [S II] ratio has two practical advantages for the determination of  $n_e$ : for  $z < 0.3$  the two [S II] lines fall in the rest-frame optical range and are hence easily observed, and the lines have a small enough separation and are thus not sensitive to reddening correction. The [O III]  $\lambda 5007/\lambda 4363$  ratio is sensitive to density as well as temperature. The 5007 and 4363 lines have different critical densities, and at densities of  $\geq 10^6 \text{ cm}^{-3}$ , the 5007 line is heavily suppressed because of the collisional de-excitation of the  $^1\text{D}_2$  level (Osterbrock & Miller 1975). Because of the different critical densities of the line transitions, the [O III] ratio is no longer a valid thermometer in the high-density (i.e.  $\geq 10^6 \text{ cm}^{-3}$ ) regions usually seen in broad-line regions (BLRs; e.g. Ho 2008). However, considering that the average physical aperture coverage of the SDSS 3-arcsec diameter fibres for galaxies at  $z > 0.02$  (cf. Table 1) is much larger than the typical size scale of the BLRs, the [O III] ratio is therefore still a reasonable temperature estimator in our case. Moreover, although the [O III] ratio is relatively sensitive to reddening correction because of the significant line separation, the mean impact for temperature measurements is no more than 10 per cent in our sample. In this study we choose to derive the electron density and electron temperature using  $I[\text{S II}] \lambda 6716/\lambda 6731$  (hereafter  $R[\text{S II}]$ ) and  $I[\text{O III}] \lambda 5007/\lambda 4363$  (hereafter  $R[\text{O III}]$ ), respectively.

The calculations of electron density and temperature are processed with the current atomic data<sup>4</sup> using the TEMDEN task

<sup>4</sup> References are listed at <http://www.noao.edu/noao/staff/shaw/nebular>

**Table 5.** Mean values of redshift,  $A_V$ ,  $\text{FWHM}_{\text{Balmer}}$  ( $\text{FWHM}_B$ ; km s $^{-1}$ ) and luminosity ( $L_{\odot}$ ) of the three classes: NLR-dominated (ND), disc-contaminated NLR (DNL and DNR; refer to Fig. 3) and non-NLR (NN) objects.

Class	Number	Redshift	$A_V$	$\text{FWHM}_B$	$\log L_{[\text{O III}]}$	$\log L_{\text{H}\beta}$	Sample A	Sample B	Sample C
ND <sub>SY</sub>	75	0.033	1.03	386	8.25	7.41	30	25	20
ND <sub>L</sub>	2	0.033	2.16	497	8.69	8.09			2
ND <sub>C</sub>	21	0.034	1.67	379	8.09	8.17		2	19
ND <sub>SF</sub>	1	0.041	2.20	306	8.21	8.86			1
DNL <sub>SY</sub>	637	0.118	0.66	394	8.34	7.54	104	135	398
DNL <sub>L</sub>	429	0.096	0.94	451	7.82	7.50	1	3	65
DNL <sub>C</sub>	69	0.118	0.97	378	8.06	8.04	9	30	274
DNL <sub>SF</sub>	11	0.140	1.20	351	8.30	8.47	3	13	118
DNR <sub>SY</sub>	313	0.108	1.11	449	9.00	8.16	139	107	183
DNR <sub>L</sub>	49	0.076	1.66	494	8.66	8.46		2	9
DNR <sub>C</sub>	134	0.102	1.75	373	9.00	8.95	2	3	44
DNR <sub>SF</sub>	33	0.122	1.39	335	9.01	8.97	7	51	21
NN <sub>SY</sub>	701	0.084	0.66	234	7.95	7.24	98	152	451
NN <sub>L</sub>	13	0.048	0.84	234	7.01	6.71			13
NN <sub>C</sub>	955	0.087	0.90	218	7.68	7.70	22	47	886
NN <sub>SF</sub>	11 576	0.075	0.68	151	7.45	7.41	519	777	10 280

within the IRAF<sup>5</sup> STSDAS package<sup>6</sup> (Shaw & Dufour 1995). The task is based on the five-level atom program first developed by de Robertis, Dufour & Hunt (1987), including diagnostics from a greater set of ions and emission lines, particularly those in the ultraviolet satellite (e.g. *International Ultraviolet Explorer* and *Hubble Space Telescope*) archives.

We treat samples A, B and C in a uniform way, except for sample C, which had poor [O III]  $\lambda 4363$  detections. That is, first we apply the uncertainty measurements of [O III]  $\lambda 4363$  to calculate the upper limits of the  $R[\text{O III}]$  ratio at a  $1\sigma$  uncertainty, before performing the plasma diagnostics. In other words, the sample C temperatures are correspondingly lower limits because higher  $R[\text{O III}]$  ratios lead to lower  $T_e$ . Higher assumed temperatures correspond to lower electron densities, and vice versa. Our plasma diagnostics are calculated as follows.

(i) The initial estimate of  $n_e$  is obtained with the [S II] ratio assuming, for example,  $T=10\,000$  K (for those with  $1.43 < R[\text{S II}] < 1.47$ , some lower values of  $T$  are assumed).

(ii) This density is then used to derive  $T_e[\text{O III}]$ . If this differs from the initial value of  $T$  by more than 10 per cent, a new value of  $n_e$  is then derived using the  $T_e[\text{O III}]$  obtained.

Note that because the density-sensitive tracer  $R[\text{S II}]$  used here is easily excited in a range of physical environments, we suggest that the  $n_e$  estimates should be considered as the mean values of the sampled regions because of the multi-phase nature of the ISM. Correspondingly, the value of  $T_e$  derived from  $R[\text{O III}]$  with  $n_e$  from  $R[\text{S II}]$  will be biased to higher values. Given  $n_e \leq 10^5$  cm $^{-3}$ , the offsets would generally be no more than 2000 K as long as  $T_e < 20\,000$  K (e.g. Osterbrock & Ferland 2006). Therefore, we claim that the diagnostics applied compose the most acceptable and feasible methodology for analysing a large SDSS sample such as ours.

At an assumed temperature or density, there are some objects

**Table 6.** Summary of objects that have ' $T_e$  with [O III] and  $N_e$  with [S II]' (TONS). The four cases are: TONS<sub>1</sub>, the calculation using the two line ratios leads to no consistent result; TONS<sub>2</sub>,  $R[\text{S II}] > 1.47$ , and thus there are no density results; TONS<sub>3</sub>,  $R[\text{O III}] < 11.1$ , and thus there are no temperature results; TONS<sub>4</sub>, both density and temperature determinations fail.

	TONS <sub>1</sub>	TONS <sub>2</sub>	TONS <sub>3</sub>	TONS <sub>4</sub>	Total
ASY(371)	12	1	1		14
AL(1)					
AC(33)	3		2		5
ASF(529)	96	47			143
Total(934)	111	48	3		162
BSY(419)	17	5	1		23
BL(5)		1			1
BC(82)	14	3	5		22
BSF(795)	204	104	14	2	324
Total(1301)	235	113	20	370	
CSY(1052)	51	37			88
CL(89)	13	2	2		17
CC(1223)	181	71	17	1	270
CSF(10 420)	3462	2328	101	35	5926
Total(12 784)	3657	2438	120	36	6251

labelled as 'TONS', which is short for ' $T_e$  with [O III] and  $N_e$  with [S II]'; this designation means that no (consistent) results were found using the simultaneous calculation processes (see Table 6). For example, it is noticeable that 2541 CSF (i.e. sample C star-forming galaxies) show  $T_e > 1.5 \times 10^4$  K (cf. columns 11 and 12 of Table 7), while 1742 (~ 70 per cent) of these are actually TONS<sub>1</sub> (1109) or TONS<sub>2</sub> (633) objects. Therefore, we further check the intensity ratios of these TONS objects.

For the TONS<sub>2</sub>, TONS<sub>3</sub> and TONS<sub>4</sub> objects, using the uncertainty measurements of the [S II] and [O III] lines to calculate the lower limits of  $R[\text{S II}]$  and the upper limits of  $R[\text{O III}]$ , we find that ~ 80 per cent of both TONS<sub>2</sub> and TONS<sub>3</sub> along with all TONS<sub>4</sub> objects show computable ratios. For the remaining 20 per cent of TONS<sub>2</sub> and TONS<sub>3</sub> objects, we suggest that the uncertainties introduced by [O III] extinction corrections have the greatest impact.

<sup>5</sup> IRAF is distributed by the National Optical Astronomy Observatories, which are operated by the Association of Universities for Research in Astronomy under cooperative agreement with the National Science Foundation.

<sup>6</sup> Available at [http://www.stsci.edu/institute/software\\_hardware/stsdas](http://www.stsci.edu/institute/software_hardware/stsdas)

**Table 7.** Summary of the physical conditions (density and temperature). Note that by applying our determination procedures, the sample C temperatures are the lower limits.  $N_s$  denotes the number of objects with  $R[\text{S II}] > 1.47$  (i.e. the upper limit for TEMDEN calculation using  $R[\text{S II}]$ ).  $N_o$  denotes the number of objects with  $R[\text{O III}] < 11.1$  (i.e. the lower limit of  $R[\text{O III}]$  for TEMDEN calculation).  $N_{1.5}$ (per cent) is the number of objects with  $1.5 < T_e < 2.0$  ( $10^4$  K) and the fraction of the corresponding subsamples.  $N_{2.0}$ (per cent) is the number of objects with  $T_e > 2.0$  ( $10^4$  K) and the fraction of the corresponding subsamples.

Object (1)	Num. (2)	R[S II]		Electron density $n_e$ ( $\text{cm}^{-3}$ )		R[O III]		Electron temperature $T_e$ ( $10^4$ K)			
		Range (3)	$N_s$ (4)	Range (5)	Median/Mean (6)	Range (7)	$N_o$ (8)	Range (9)	Median/Mean (10)	$N_{1.5}$ (per cent) (11)	$N_{2.0}$ (per cent) (12)
ASY	371	0.81-1.47	1	6-1620	422/447	8.8-2E2	1	0.5-5.7	1.5/1.7	154(42)	45(12)
AL	1	0.73		3959		14.2		5.4			1(100)
AC	33	1.06-1.45		2-624	168/204	7.3-2E2	2	1.0-7.5	1.9/2.2	7(21)	13(39)
ASF	529	0.96-1.71	45	1-780	62/79	14.3-3E2	0	0.7-5.5	1.2/1.2	25(5)	3(<1)
BSY	419	0.81-1.71	5	3-1465	332/360	8.3-2E2	1	0.7-8.1	1.5/1.6	173(41)	38(9)
BL	5	0.83-1.48	1	76-2244	508/777	17.0-6E1		1.7-4.2	1.8/2.3		5(100)
BC	82	0.85-1.55	3	3-1301	181/230	2.9-3E2	5	0.9-7.5	2.0/2.2	16(20)	39(48)
BSF	795	0.93-2.85	104	1-1108	42/69	1.2-3E2	16	0.6-8.2	1.1/1.3	36(5)	31(4)
CSY	1052	0.80-2.05	37	1-1499	216/256	20.7-7E3		0.4-2.6	1.1/1.1	69(7)	6(<1)
CL	89	1.00-1.49	2	3-609	172/187	6.7-7E2	2	0.6-6.5	1.3/1.7	14(16)	22(25)
CC	1223	0.87-1.66	72	1-1410	134/169	6.0-9E3	18	0.4-8.9	1.3/1.6	244(20)	244(20)
CSF	10 420	0.86-2.53	2361	1-1141	32/55	4.1-6E5	136	0.3-10.0	1.0/1.4	1104(10)	1437(14)

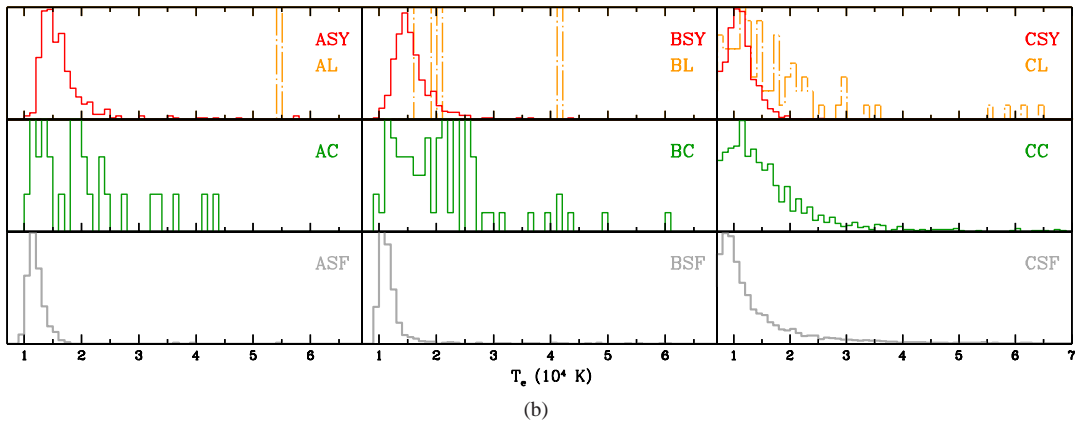
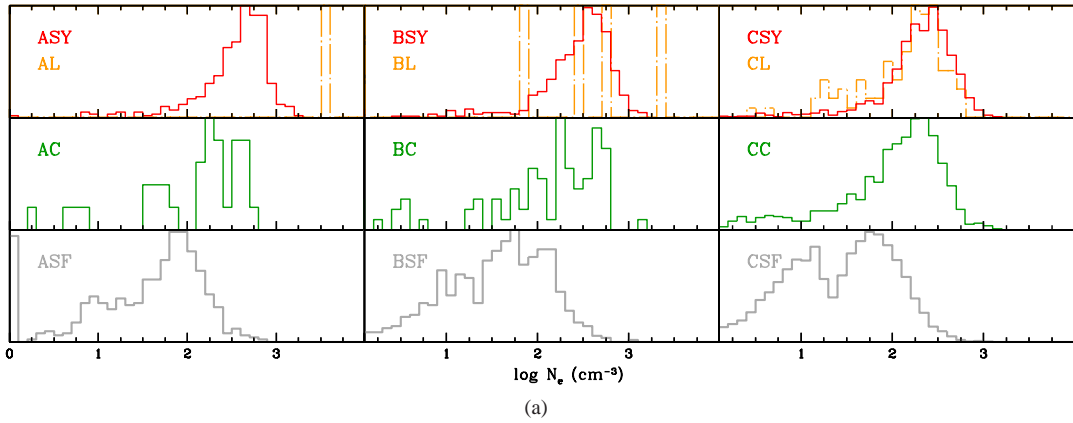


**Figure 4.** Normalized histograms of electron density (a) and electron temperature (b). For each panel, from top to bottom, we show Seyferts (red solid) and LINERs (orange dot-dashed), composites (darkgreen), and star-forming galaxies (grey), and from left to right, we show samples A, B and C.

Therefore, these three cases are most likely introduced by observational uncertainties. In the  $\text{TONS}_1$  cases, we suggest an additional possibility, that the intrinsically different spatial distributions of the [S II] and [O III] emitting regions might lead to inconsistent results in the calculations of  $n_e$  and  $T_e$ .

The plasma diagnostic results are summarized in Table 7, and Fig. 4 shows the normalized histograms of  $n_e$  and  $T_e$ . The main results are as follows.

*Electron density.* Considering the density results, we can see a clear sequence (cf. columns 5 and 6 of Table 7):  $n_{\text{LINER}} \gtrsim n_{\text{Seyfert}}$



$> n_{\text{composite}} > n_{\text{star-forming}}$ . The typical  $n_e$  uncertainties are  $150 \text{ cm}^{-3}$  for Seyferts, LINERs and composites, and  $80 \text{ cm}^{-3}$  for star-forming galaxies. Comparing samples A, B and C, the CSY and CL possess significantly lower  $n_e$  ( $\sim 150 \text{ cm}^{-3}$ ) than A/BSY and A/BL, most likely indicating some effect of shocks in strong [O III]  $\lambda 4363$  emitters (please refer to Table 2 for the abbreviations). The characteristic  $n_e$  range of active galaxies, including Seyferts, LINERs and composites, is  $10^{2-3} \text{ cm}^{-3}$ , while that of the star-forming galaxies is  $10^{1-2} \text{ cm}^{-3}$ . As shown in Fig. 4(a), the  $n_e$  sequence mentioned above is visible. However, we see a bimodal number distribution of  $n_e$ , which is especially significant for star-forming galaxies. To check whether this is a real effect, we examine the  $R[S II]$  distribution and we can confirm no corresponding bimodality. In fact, the typical uncertainty for objects with  $n_e < 10$  is  $\sim 40 \text{ cm}^{-3}$  in our sample. As a result, the bimodal distribution is most likely introduced by the algorithm used for calculating the electron density in the TEMDEN package and is therefore not a physical real effect.

**Electron temperature.** The temperature results are listed in Table 7 (cf. columns 9 to 12). Fig. 4(b) shows normalized temperature histograms for each galaxy type. As given above, sample C temperatures should be viewed as the lower limits for comparison. First, a  $T_e$  sequence is clearly shown:  $T_{\text{LINER}} \gtrsim T_{\text{composite}} > T_{\text{Seyfert}} > T_{\text{star-forming}}$ . The typical uncertainties of  $T_e$  for the four galaxy classes are (in units of  $10^4 \text{ K}$ ) 0.2 for Seyferts, 0.3 for LINERs, 0.5 for composites and 0.1 for star-forming galaxies. Secondly, the sampled LINERs display a mean  $T_e$  of approximately  $2 \times 10^4 \text{ K}$  (cf. column 10 of Table 7) and show the highest number fraction of high  $T_e$  species (i.e.  $T_e > 1.5 \times 10^4 \text{ K}$ ; cf. column 11 and 12 of Table 7). Thirdly, a remarkable result is that the composites as a group show a value of  $T_e$  very close to that of the LINERs and approximately 5000 K higher than that of the Seyferts. This result reveals the existence of very different dominating ionizing source(s) in composites from those in star-forming galaxies. For star-forming galaxies, the derived temperatures are generally consistent with the classical diagnostic results of bright planetary nebula ( $\sim 1.1 \times 10^4 \text{ K}$ ). Moreover, as revealed in Fig. 4, the active galaxies (e.g. LINERs and composites) show a significant tail extending to much higher temperatures, up to  $6 \times 10^4 \text{ K}$ , which is far too high to be explained only by photoionization caused by stars.

## 5 ELECTRON DENSITY AND ELECTRON TEMPERATURE IN NLRs

**Electron density in NLRs.** As shown in Fig. 5, most NLRs lie in the  $n_e$  range of  $10^{2-3} \text{ cm}^{-3}$ . Only seven Seyferts, seven composites and one LINER have lower values of  $n_e$ , some of which might be the result of flux measurement uncertainties. We have tried higher densities of  $10^{5-6} \text{ cm}^{-3}$  to calculate  $T_e[\text{O III}]$  for our selected NLRs, but a significant fraction of Seyferts show values no greater than 6000 K, which could not be representative of the cases of NLRs of AGNs found in the literature (e.g. Bennert et al. 2006). Thus, our results suggest that the characteristic  $n_e$  range in NLRs of active galaxies is  $10^{2-3} \text{ cm}^{-3}$ .

**Electron temperature in NLRs.** As illustrated in Fig. 5, the typical range of  $T_e$  in Seyferts is  $1.0\text{--}2.0 \times 10^4 \text{ K}$ , with a median value of  $1.4 \times 10^4 \text{ K}$ . Because both the selected LINERs and composites contain larger fractions of sample C objects than the Seyferts, and the  $T_e$  derived could thus be biased to lower values, the typical range of these two classes could be higher and wider than that shown in Fig. 5.

Fig. 6 plots  $n_e$  (top) and  $T_e$  (bottom) as functions of physical

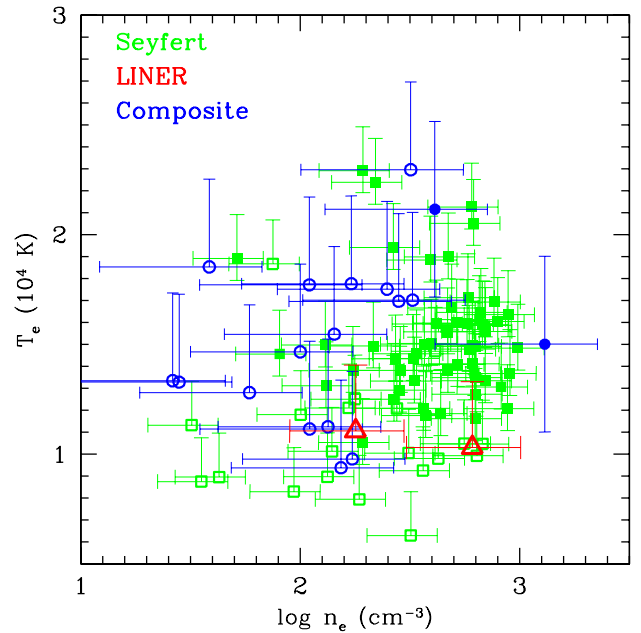


**Figure 5.** Electron density versus electron temperature. Sample distribution of the NLR-dominated objects: Seyferts (blue boxes), LINERs (red triangles) and composites (green circles), with error bars showing  $1\sigma$  dispersions. Open symbols denote objects from sample C with lower  $T_e$  limits.

aperture size  $\ln\phi$  for Seyferts in bins of  $\ln\phi$ . For a precise evaluation, we further calculate the mean values of  $n_e$  and  $T_e$  for different types of objects. As shown in Table 8, the  $n_e$  and  $T_e$  of Seyferts show transitions from the NLR to the disc:  $n_{\text{NDSY}} > n_{\text{DNRSY}} > n_{\text{DNL SY}} > n_{\text{NN SY}}$  and  $T_{\text{NDSY}} > T_{\text{DNRSY}} > T_{\text{DNL SY}} > T_{\text{NN SY}}$  (refer to Table 5 for the classifications). The unexpected low value of  $T_e$  for NLR-dominated NLR LINERs and the high value of  $T_e$  for non-NLR LINERs can most likely be explained by selection biases: the former is a result of the small sample size (i.e. only two from sample C) and the latter is because the non-NLR LINERs are sampled at lower redshifts than the disc-contaminated NLR LINERs and are biased to regions close to the galaxy centres. For composites and star-forming galaxies, we find no clear transition, as seen in the Seyferts. Therefore, we have checked further and found that this result was due to misclassification; that is, the correlation (see equation 2) found by Bennert et al. (2002) was derived from Seyferts.

We have reported single and statistical estimates of  $n_e$  and  $T_e$  for the NLRs of active galaxies. Physically, the emission-line regions are, by their nature, multi-phase media, and thus densities and temperatures are strongly coupled with non-uniformity. When modelling the NLRs, both density and temperature could vary with different physical conditions, and such non-uniformity or multi-phase nature should be considered (e.g. Binette, Wilson & Storchi-Bergmann 1996; Komossa & Schulz 1997; Baskin & Laor 2005). We will leave this discussion to a companion paper, which will focus on modelling.

### 5.1 High- $T_e$ NLRs in line-ratio diagnostic diagrams

One item remaining in the problem of modelling of NLR is the so-called temperature problem: the difficulty in reproducing high  $T_e[\text{O III}]$  with photoionization models. For instance, (Heckman & Balick 1979) have claimed that  $T_e > 20\,000 \text{ K}$  requires a source of energy in addition to photoionization. Traditionally, two different av-



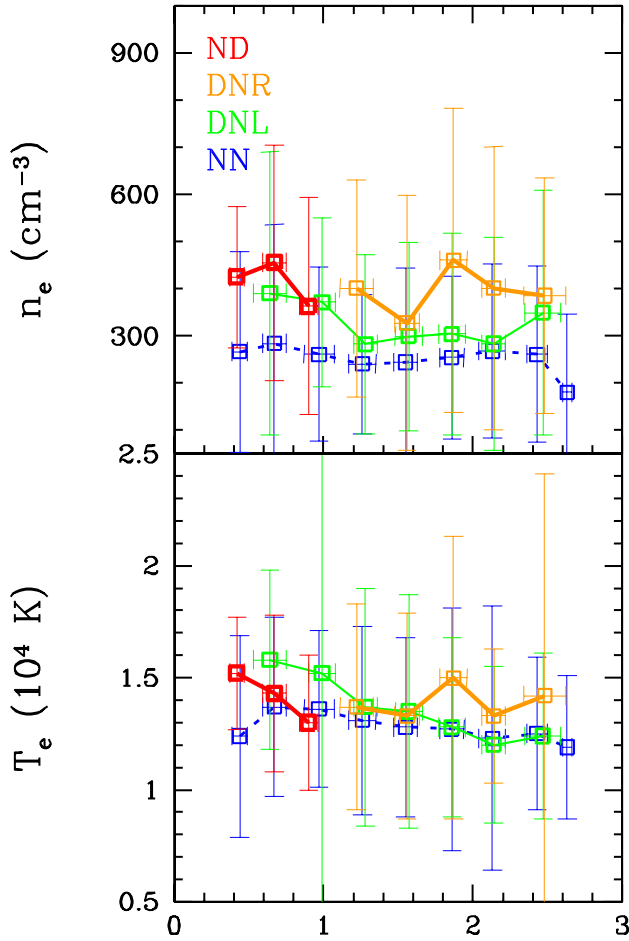


**Figure 6.** Physical aperture size  $\ln\phi$  versus  $n_e$  (top) and  $T_e$  (bottom) for Seyferts in bins of  $\ln\phi$ . Empty boxes are the median values of  $\ln\phi$ ,  $n_e$  and  $T_e$ , with error bars showing  $1\sigma$  dispersions: NLR-dominated (ND, red), disc-contaminated NLR (DNR, orange; DNL, green thin; refer to Fig. 3) and non-NLR objects (NN, dashed blue).

**Table 8.** Mean  $n_e$  and  $T_e$  of the NLR-dominated (ND), the disc-contaminated NLR (DNL and DNR) and the non-NLR (NN) objects. Strong (sample A), intermediate (sample B) and weak (sample C) [O III] $\lambda$ 4363 objects are all included. For classifications, please refer to Fig. 3.

	$n_e$ ( $\text{cm}^{-3}$ )				$T_e$ ( $10^4$ K)			
	ND	DNR	DNL	NN	ND	DNR	DNL	NN
SY	427	394	306	255	1.40	1.39	1.28	1.29
L	394	413	244	92	1.07	1.75	1.73	1.87
C	197	166	151	167	1.54	1.63	1.71	1.61
SF	109	148	94	44	1.78	1.44	1.93	1.32

enues have been explored when modelling the NLRs: photoionization and shock ionization. It is generally believed that photoionization is the dominant excitation mechanism in most AGNs, while the intrinsic defect of all shock models (e.g. Allen et al. 2008) is that they require shocks throughout the NLR and that they cannot, alone, explain all NLR emission because shock signatures cannot always be observed. There have been several previous to solve the temperature problem from different perspectives (e.g.

Binette, Wilson & Storchi-Bergmann (1996)). Here, we compare some of the current models with our selected high- $T_e$  object data.

Line-ratio diagnostic diagrams are commonly used to visualize and compare models with observations. The ratios of emission lines plotted against one other, depending upon the emission lines chosen, can show clear relationships in density, metallicity, and the ionization mechanism. For example, [O III]  $\lambda$ 5007/[O II]  $\lambda$ 3726,29 (hereafter [O III]/[O II]) is theoretically independent of the chemical abundance and is a very good indicator of the ionization parameter. [O I]  $\lambda$ 6300/H $\alpha$  (hereafter [O I]/H $\alpha$ ) is sensitive to the ionization parameter. [O III]  $\lambda$ 5007/H $\beta$  (hereafter [O III]/H $\beta$ ) depends on all the parameters but is also frequently used as an indicator of the ionization parameter. [N II]  $\lambda$ 6584/H $\alpha$  (hereafter [N II]/H $\alpha$ ) is mostly sensitive to the gaseous abundance. [S II]  $\lambda$ 6716,31/H $\alpha$  (hereafter [S II]/H $\alpha$ ) is sensitive to the density. The ionization parameter  $U$  is defined as

$$U = \frac{Q_{\text{tot}}}{4\pi r^2 n c} \quad (3)$$

where  $Q_{\text{tot}}$  is the total number rate of hydrogen ionizing photons isotropically emitted by the nucleus,  $r$  is the representative distance of the emission-line clouds from the central source and  $n = n_H$  is the total hydrogen number density. We calculate the extinction correction effects on multiple line ratios: [N II]/H $\alpha$ , [O III]/H $\beta$ , [S II]/H $\alpha$ , [O I]/H $\alpha$ , [O III]/[O II] and the temperature-sensitive [O III] ratio. The [O III]/[O II] ratio is the most sensitive to extinction correction, showing a  $\sim 30$  per cent decrease after the extinction correction, and the temperature-sensitive [O III] ratio decreases less than 10 per cent.

Fig. 7 shows the NLR observations on the line-ratio diagrams. Here we select four frequently used line-ratio diagnostic diagrams: [N II]/H $\alpha$  versus [O III]/H $\beta$ , [S II]/H $\alpha$  versus [O III]/H $\beta$ , [O I]/H $\alpha$  versus [O III]/H $\beta$  and [O III]/[O II] versus [O III]/H $\beta$ . The observational data points are the NLR-dominated objects in A/BSY (i.e. sample A/B Seyferts) with  $T_e > 15\,000$  K (crosses). The model grids are plotted using ITERA<sup>7</sup>, which is an IDL tool for emission-line ratio analysis (refer to Groves & Allen 2010 for details). The metallicities shown in the side bar are in units of solar metallicity.

Temperature and ionization are fundamentally determined by the ionization source. First, we try both AGN (Groves, Dopita & Sutherland 2004a,b) and shock (Allen et al. 2008) model libraries, which are currently available with ITERA. The former are photoionization models of the NLRs of AGN, while the latter consider fast shock effects. We find that the AGN models fit our observations better. Previous observations indicate that the NLR clouds are likely to be dusty and clumpy in nature. The dusty AGN models consider this effect to produce a physical model to explain why and how the AGN NLRs cluster on line ratio diagrams: dust dominates the opacity in dusty gas at high  $U$ , and the gas pressure gradient must match the radiation pressure gradient in isobaric systems. Therefore, these assumptions lead to a self-regulatory mechanism for the local ionization parameter and hence for the emission lines. We have conducted further experiments and found that the dusty, radiation-pressure dominated, photoionized AGN model grids can best reproduce our data when assuming a gas density of  $n_H = 100 \text{ cm}^{-3}$  and a power-law index  $\alpha = -1.4$ . In Fig. 7, we can see that the observed flux ratios are generally well described by the dusty AGN model predictions.

<sup>7</sup> ITERA, and associated libraries and routines are all available from <http://www.brentgroves.net/itera.html>

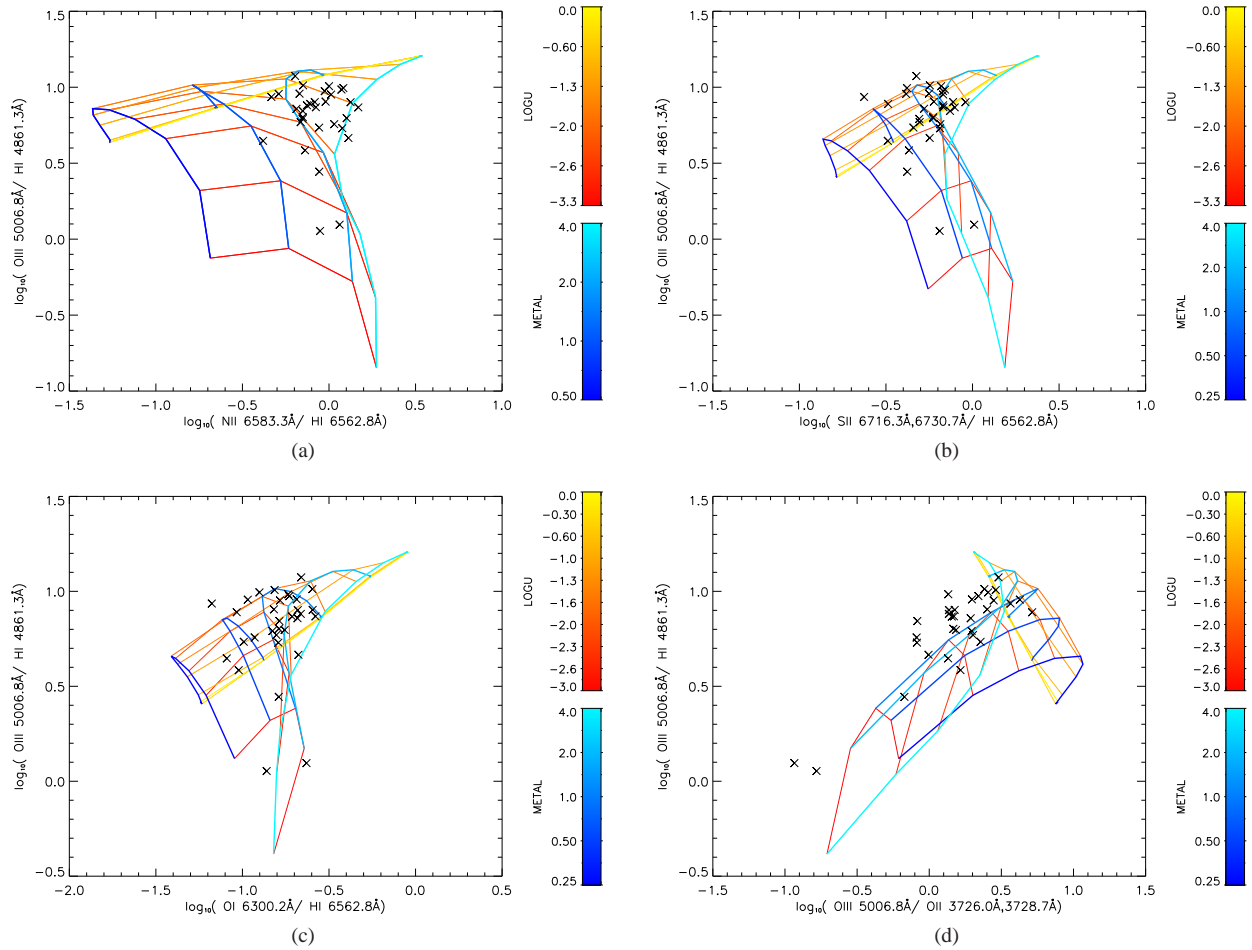


**Figure 7.** Four panels show selected diagnostic diagrams in which models and observations are compared: (a) the [N II]/H $\alpha$  versus [O III]/H $\beta$  diagram; (b) the [S II]/H $\alpha$  versus [O III]/H $\beta$  diagram; (c) the [O I]/H $\alpha$  versus [O III]/H $\beta$  diagram; (d) the [O III]/[O II] versus [O III]/H $\beta$  diagram. The observational data points (black crosses) are the NLR-dominated objects in A/BSY (i.e. sample A/B Seyferts) with  $T_e > 15\,000$  K. The model grids are plotted using ITERA, showing dusty, radiation-pressure dominated photoionized AGN models. We assume electron density of  $100\text{ cm}^{-3}$  and the power-law index  $\alpha = -1.4$ . The metallicity is in unit of solar metallicity.

However, some remaining problems still need to be addressed, as follows.

(i) Our NLR data present a characteristic  $n_e$  range of  $10^{2-3}\text{ cm}^{-3}$ . The fact that the dusty AGN grids fit the data with density  $n_H = 100\text{ cm}^{-3}$  better than other density constraints is illustrative.

(ii) Despite the overall good fitting, the model grids present a systematic overestimation by a factor of 2 in the [O III]/[O II] versus [O III]/H $\beta$  diagram. [O III]/[O II] is sensitive to extinction correction and it decreased by approximately 30 per cent after correction. Even when including the uncertainties introduced by extinction corrections, the remaining discrepancy is still remarkable.

(iii) Although emission line ratios support photoionization as the dominant ionization mechanism, the high gas temperatures and velocities observed within the NLR indicate that shocks might play a part in this region (see the discussion in Section 7.2).

(iv) Some of these high- $T_e$ , strong [O III] $\lambda$ 4363 emission Seyfert 2 galaxies show low-metallicity (i.e.  $Z/Z_\odot \sim 1$ ; see the discussion in Section 7.3).

To proceed, we will try to physically model the NLRs and probe these problems in a companion paper.

## 6 $M_\star$ AND $\text{SFR}/M_\star$

The electron density and temperature are quantities representing the current statuses of NLRs, while stellar mass ( $M_\star$ ) and star formation rate per unit mass (i.e. the specific star formation rate,  $\text{SFR}/M_\star$ ) provide information about the galaxy formation histories. Either stellar mass is conserved or it is a slowly increasing quantity unaffected by morphological transformations and mergers (e.g. Hopkins et al. 2009). Traditionally, the masses of galaxies are estimated by dynamical methods from the kinematics of their stars and gas. The specific star formation rate has either explicitly or implicitly been used in numerous studies of field galaxies at  $z < 1$ . It defines a useful measure of the rate at which new stars add to the assembled mass of a galaxy (i.e. a characteristic time-scale of star formation) and it is strongly related to several other important physical quantities (e.g. Clark & Oey 2002).

We adopt  $M_\star$  and  $\text{SFR}/M_\star$  derived using the methodologies of Kauffmann et al. 2003a and Brinchmann et al. 2004, respectively. Kauffmann et al. (2003a) have constrained the stellar masses of galaxies using two stellar absorption-line indices (the 4000-Å break strength  $D_n4000$  and the Balmer absorption-line index  $H\delta_A$ ). Brinchmann et al. (2004) have obtained the SFR and  $\text{SFR}/M_\star$  by two means: for star-forming galaxies, they used the observed H $\alpha$

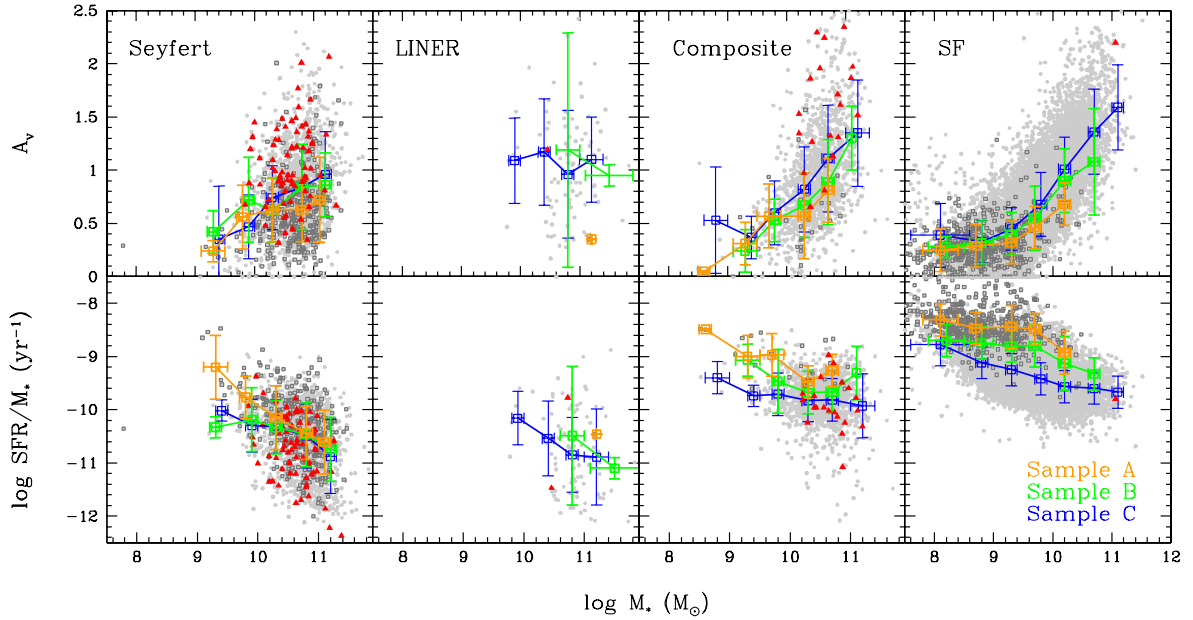


**Figure 8.** Stellar mass  $M_*$  versus dust attenuation  $A_V$  (top) and specific star formation rate  $\text{SFR}/M_*$  (bottom) in bins of  $M_*$ . Empty boxes are the median values of  $M_*$ ,  $A_V$  and  $\text{SFR}/M_*$ , with error bars showing  $1\sigma$  dispersions. From left to right: Seyferts, LINERs, composites and star-forming galaxies. Each type of galaxies is divided into sample A (orange), sample B (green) and sample C (blue). Red triangles are the NLR-dominated objects, dark grey open squares present the distribution of the sample A objects and grey background indicates the remaining objects (please refer to the online figure for details).

luminosity and converted this into a SFR, while for composites and AGNs, they used a calibration based on  $D_n4000$ . The sample they used was drawn from SDSS DR2 with essentially all aperture bias removed. Note that their results are based on a model grid (Charlot et al. 2002), ensuring a consistent picture for the attenuation of continuum and line emission photons.

In this section, we turn our attention to  $M_*$  and  $\text{SFR}/M_*$  and we analyse both the relations between the two properties for different classes and their relations with the obtained plasma diagnostic results. Then, we compare these physical properties of the NLRs to those of the host galaxies.

### 6.1 $M_*$ versus $\text{SFR}/M_*$

It is interesting to plot  $\text{SFR}/M_*$  as a function of  $M_*$ . Previous studies have shown that galaxies generally split into two basic populations: concentrated galaxies with low  $\text{SFR}/M_*$  and low-mass, less concentrated galaxies with high  $\text{SFR}/M_*$  (e.g. Kauffmann et al. 2003b; Brinchmann et al. 2004). However, this is far from the full story. Salim et al. (2007) have constructed a two-dimensional probability distribution function in the  $(\log \text{SFR}/M_*, \log M_*)$  plane and found that different types of emission-line galaxies occupy relatively distinct portions of the parameter space. Here, we attempt to provide more details.

(i) Fig. 8 (bottom panels) shows that the  $\text{SFR}/M_*$  of the star-forming galaxies slowly decreases with increasing  $M_*$  from approximately  $10^8$  to  $10^{11} M_\odot$ , while those with high  $M_*$  show a much less pronounced correlation. Interestingly, those ‘less active’ galaxies are indeed active galaxies: Seyferts and LINERs. Most composites are located at the junction connecting the AGN and star-forming branch. The distribution pattern agrees well with that presented by Salim et al. 2007.

(ii) As shown in Table 3, objects with high  $A_V$  (e.g. sample C composites), generally reside in the conjoining region. They

have a much higher  $A_V$  than the Seyferts at constant  $M_*$ . In general, high mass galaxies are older than low-mass galaxies, at a fixed stellar mass, studies show that high SFR galaxies yield relatively younger populations than those with lower SFR (e.g. Schaerer, de Barros & Sklias 2012). In other words, galaxies with lower  $\text{SFR}/M_*$  along with higher  $M_*$ , on average, have experienced active star-forming activities and therefore are intrinsically older (e.g. Heavens et al. 2004). Given that the amount of dust produced is proportional to the amount of stellar mass, as shown in the top panels in Fig. 8, we speculate that some wide-reaching mechanisms (e.g. outflows driven by the AGN) might act to blow out dusty gases or consume a significant fraction of the dust content while lowering the  $\text{SFR}/M_*$  for massive galaxies.

(iii) The selected NLR-dominated objects are plotted in Fig. 8 (red solid squares), contrasting with the background host galaxies (grey dots). In the  $(\log M_*, \log \text{SFR}/M_*)$  parameter planes, the NLRs distribute uniformly with the host galaxies, only biasing unsurprisingly to higher masses for the composites, because they reside in massive active galaxies by nature. To be observed, optical SFRs require emission-line luminosities and thus the aperture effects on emission-line luminosities can lead to strong biases in star-formation rate studies. In the  $(\log M_*, A_V)$  plane, we observe that the NLRs-dominated objects, on average, present higher  $A_V$  values, which is also expected. Brinchmann et al. (2004) have proposed an aperture correction method and have calculated the likelihood distribution of the SFR for a given set of spectra with global and fibre  $g-r$  and  $r-i$  colours. They have proposed that their correction method is robust, only if  $\geq 20$  per cent (a criterion argued by Kewley, Jansen & Geller 2005) of the total  $r$ -band light is sampled by the fibre; thus, a redshift  $z > 0.04$  is required for SDSS. However, as given in Section 5, only systems with  $\ln\phi < 1$  (i.e.  $z < 0.046$ ) are considered to be NLR-dominated. With these considerations, no precise conclusion can yet be reached, and further specific observations might be helpful.

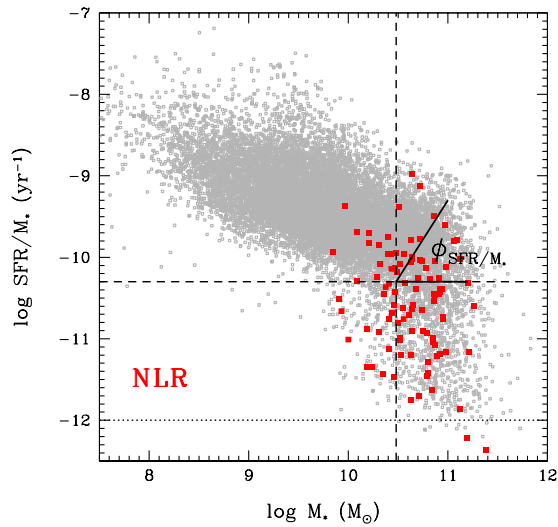


**Figure 9.** Sample distributions on the  $M_*$  versus  $SFR/M_*$  diagram, where red solid squares denote the NLR-dominated objects and grey squares indicate the remaining objects. The dashed lines indicate  $\log M_* = 10.48$  (i.e.  $M_* = 3 \times 10^{10} M_\odot$ , vertical) and  $\log SFR/M_* = -10.30$  (i.e.  $SFR/M_* = 5 \times 10^{-11} \text{ yr}^{-1}$ , horizontal). The dotted line presents  $\log SFR/M_* = -12$ .

(iv) Finally, active galaxies with strong [O III]  $\lambda 4363$  emission behave unexpectedly. A/BSY and A/BL distribute uniformly with CSY/L, and A/BC are located on the high  $SFR/M_*$  side with lower  $M_*$  compared to CC objects (refer to Table 2 for the abbreviations). Meanwhile, the situations are quite different in the star-forming cases: A/BSF definitely have both much lower  $M_*$  and higher  $SFR/M_*$  compared to CSF objects. As we have previously understood, strong [O III]  $\lambda 4363$  emissions in star-forming galaxies imply high  $T_e$  and low cooling efficiency, and thus low gaseous metallicity; therefore, these objects have higher  $SFR/M_*$  than weak [O III]  $\lambda 4363$  emission star-forming galaxies at constant  $M_*$ . However, this reasoning will not work in the AGN cases. Taking the Seyferts as an example, it seems that the occurrence of strong [O III]  $\lambda 4363$  emission is just a matter of frequency: there is no significant separation between the strong (i.e.  $S/N > 5$ ) and weaker (i.e.  $1 < S/N < 5$ ) [O III]  $\lambda 4363$  Seyferts in the  $(\log M_*, \log SFR/M_*)$  plane, compared to composites and star-forming galaxies. In addition, the strong [O III]  $\lambda 4363$  Seyferts distribute in a much wider range of  $SFR/M_*$  (i.e.  $-10.6 < SFR/M_* < -9.2$ ) than the corresponding star-forming ones (i.e.  $-9 < SFR/M_* < -8.2$ ). Assuming that the classifications of narrow emission-line galaxies are correct, we believe that such significantly different distribution patterns reveal some intrinsic physics related to [O III]  $\lambda 4363$  generating mechanisms and the properties of the central energy sources in galaxies. Some studies have shown that, in general, the ionization potential of the emission region is positively correlated with the [O III]  $\lambda 4363$  flux (e.g. Nagao, Murayama & Taniguchi 2001; Vaona et al. 2012). Therefore, we refer to the results described above as the ‘evolutionary pattern of AGN with high ionization potential’. The key point is regarding the nature of the high-energy processes that excite the [O III] coronal lines in active galaxies. For example, the results from Aird et al. (2012) demonstrate that the same physical processes regulate AGN activity in all galaxies in the  $M_*$  range (i.e.  $9.5 < \log M_* < 12$ ) and could most likely be provoked by the energetically central nucleus.

**Table 9.** Summary of  $SFR/M_*$  in seven  $M_*$  bins.

$\log M_* (M_\odot)$	$SFR/M_* (\text{yr}^{-1})$			
	Seyferts	LINERs	Composites	Star-forming
8.1				-8.60
8.7			-9.04	-8.99
9.3	-9.65		-9.36	-9.17
9.8	-10.16	-10.16	-9.66	-9.57
10.3	-10.28	-10.54	-9.81	-9.56
10.7	-10.48	-10.83	-9.80	-9.60
11.2	-10.80	-10.89	-9.91	-9.70

## 6.2 Galaxy formation timescale sequence

It is now commonly accepted that the star formation history of a given galaxy depends strongly on its mass. Higher values of the specific SFR suggest that a larger fraction of stars was formed recently. The specific SFR is often called the galaxy present-day build-up time-scale, while  $M_*$  is the product of the overall galactic star-forming processes. We compare the mean  $SFR/M_*$  of the four classes in seven  $M_*$  bins. Table 9 clearly demonstrates that  $SFR/M_L \geq SFR/M_{SY} < SFR/M_C < SFR/M_{SF}$  at constant  $M_*$ . Therefore, we consider these two clues combined as an indicator of galaxy formation history: it is generally true that  $Y_L \geq Y_{SY} > Y_C > Y_{SF}$ , where  $Y$  is present-day star-formation time-scale. However, this should not be confused with an actual galaxy age, because the specific SFR tells us only how long it would have taken to build a galaxy, assuming it had a current SFR throughout its lifetime.

In Fig. 9, we plot four classes of emission-line galaxies: Seyferts, LINERs, composites and star-forming in the  $(\log M_*, \log SFR/M_*)$  plane. We define an empirical base point on the logscale  $M_*$  versus  $SFR/M_*$  diagram,  $[-10.30, 10.48]$ , which corresponds to  $M_* = 3 \times 10^{10} M_\odot$  and  $SFR/M_* = 5 \times 10^{-11} \text{ yr}^{-1}$  (marked in Fig. 9). The latter threshold is a ‘by-eye’ division, because most star-forming galaxies perfectly distribute above the vertical dashed line. Kauffmann et al. (2004) have found that the transition from a young to old stellar population takes place at a characteristic  $M_*$  of  $3 \times 10^{10} M_\odot$ , the logscale value of which is  $\sim 10.48$ . For galaxies with  $M_*$ , above this threshold, the distribution of sizes and concentrations at fixed stellar mass is independent of their local environments, and these galaxies have high stellar masses, high concentrations, high surface densities, little on-going star formation and red colours.

Now we use the base point described above as the vertex to determine the angle, which is labelled  $\phi_{SFR/M_*}$ , that each galaxy in our sample makes with the x-axis in the  $(\log M_*, \log SFR/M_*)$  plane. Fig. 10 shows the normalized histograms of this angle corresponding to different galaxy types. Notice that, for accuracy, those with log-scaled specific SFR exceeding  $-12$  are not included (i.e. objects that lie below the dotted lines in Fig. 9 are not counted because  $SFR/M_*$  estimates tend to be inaccurate past  $\sim 10^{-12} \text{ yr}^{-1}$ ; Brinchmann et al. 2004). We can see that the histograms of the Seyferts and LINERs look quite similar and both peak at  $\phi_{SFR/M_*} \sim 300^\circ$ , while composites and star-forming galaxies specify very different distributions: the former peaks at approximately  $90^\circ$  and the latter at approximately  $140^\circ$ .

## 6.3 Current status versus formation history

Utilizing previously obtained  $n_e$  and  $T_e$ , which indicate the current statuses of galaxies, along with the dust attenuation  $A_V$ , finally we



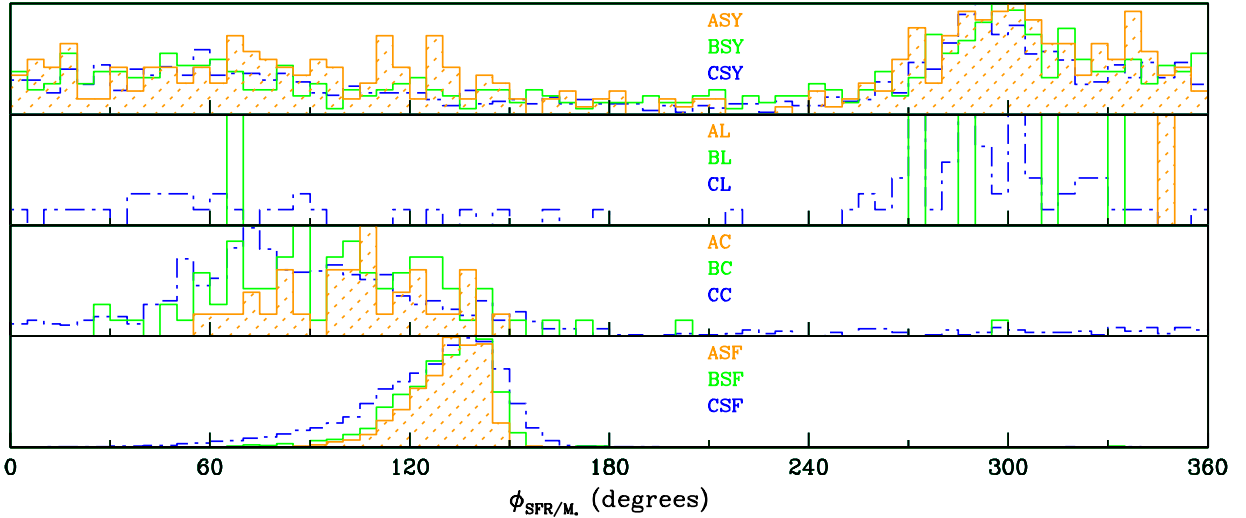


**Figure 10.** Normalized histograms of  $\phi_{\text{SFR}/M_\star}$ , which is the angle relative to the x-axis in the  $M_\star$  versus  $\text{SFR}/M_\star$  diagram, using the empirical point [-10.30, 10.48] as the vertex (see Fig. 9). From top to bottom, we show Seyferts (A/B/CSY; refer to Table 2 for the abbreviations), LINERs (A/B/CL), composites (A/B/CC) and star-forming galaxies (A/B/CSF). Blue dotted histograms show objects with  $1 < \text{S/N} < 3$  for [O III]  $\lambda 4363$ , green dot-dashed ones indicate those with  $3 < \text{S/N} < 5$  and orange solid (shaded) histograms are those with  $\text{S/N} > 5$ . Note that objects with  $\log \text{SFR} < -12$  are not included.

analyse their relations with galaxy formation history, indicated by  $M_\star$  and  $\text{SFR}/M_\star$ . Fig. 11 illustrates our sample distributions in five property pairs. We notice the following.

*Dust attenuation.* The amount of dust content shows a pronounced correlation with the amount of stellar mass (i.e. massive galaxies contain more dust). As a function of  $\text{SFR}/M_\star$ ,  $A_V$  shows a positive correlation at low  $\text{SFR}/M_\star$  and then becomes negative. Objects with  $\log \text{SFR}/M_\star \sim -10$  have the highest  $A_V$ , and the NLR-dominated objects (red triangles) have a wide range of  $A_V$  and show both high  $M_\star$  and low  $\text{SFR}/M_\star$ , compared to the host galaxies (grey dots).

*Electron density.* As a function of  $M_\star$ ,  $n_e$  also shows a positive correlation and reaches the highest value at the massive end. As a function of  $\text{SFR}/M_\star$ , a significant threshold is clearly revealed. A large fraction of objects with  $\log \text{SFR}/M_\star < -10$  have  $n_e > 100 \text{ cm}^{-3}$ , while those with  $\log \text{SFR}/M_\star > -10$  show a much wider  $n_e$  distribution. Most of the NLRs naturally lie in high  $n_e$  regions.

*Electron temperature.* Compared to both  $A_V$  and  $n_e$ ,  $T_e$  displays much less pronounced correlations with both  $M_\star$  and  $\text{SFR}/M_\star$ . The existence of an unexpected high- $T_e$  branch is quite remarkable. The branch appears at approximately  $9.5 < \log M_\star < 11$  and  $-10.4 < \log \text{SFR}/M_\star < -9.4$ . The NLRs as a group show higher  $T_e$  than the host galaxies.

A significant  $T_e$  ‘pumping-up’ is shown in Fig. 11. As listed in Table. 10, while having similar redshifts, objects with  $T_e > 2 \times 10^4 \text{ K}$  show much lower [O III]  $\lambda 5007$ . Considering that  $T_e$  increases rapidly with decreasing  $R[\text{O III}]$  (i.e.  $I[\text{O III}] \lambda 5007/\lambda 4363$ ), we infer that the plume towards high  $T_e$  is most likely the sign of an inaccurate  $T_e$  estimate at the low  $R[\text{O III}]$  end (Fig. 12). Moreover, we can see in Fig. 11 that objects from sample A and sample B form a bimodal distribution in  $M_\star$  and  $\text{SFR}/M_\star$ , which is not seen in sample C. Given that [O III]  $\lambda 4363$  correlates with galaxy activity, we argue that there exists a distinct low-activity population in active galaxies with  $9.5 < \log M_\star < 11$  and  $-10.4 < \log \text{SFR}/M_\star < -9.4$ , which might indicate some evolutionary stage.

**Table 10.** Summary of high- $T_e$  objects ( $> 2 \times 10^4 \text{ K}$ ) and low- $T_e$  objects (the rest) from samples A and B (median values). Note that [O III]<sub>63</sub> and [O III]<sub>07</sub> denote the pre-extinction correction fluxes of [O III]  $\lambda 4363$  and 5007, respectively (in units of  $10^{-17} \text{ erg/s/cm}^2$ ).

Objects	[O III] <sub>63</sub>	[O III] <sub>07</sub>	Redshift	$M_\star$	$\text{SFR}/M_\star$
High $T_e$	17	464	0.08	10.5	-9.7
Low $T_e$	17	1683	0.07	9.5	-8.9

## 7 DISCUSSION

### 7.1 Shock effects on $n_e$ and $T_e$

Stellar photoionization is not the only process that leads to the formation of emission lines. In fact, ionization can also be produced in shocks (e.g. Dopita, Groves & Sutherland 1995, 1996). To explain the observed emission line ratios, the possible contribution of shock-heating to photoionization must be examined. The cooling radiation from shocks produces high-energy photons that contribute to ionization. Kinetic energy is transformed into thermal energy, and the energetic thermal electrons can ionize the gas. Shocks are ubiquitous in galaxies. For example, shocks in AGNs can be caused by jets, winds or supersonic turbulence. Here, we find several emission line spectral indicators that can help trace the effects of shocks.

(i) The density calculations show that the strong [O III]  $\lambda 4363$  AGN density is  $100\text{--}150 \text{ cm}^{-3}$  higher than those that show no [O III] (see Section 4). Shocks generate compression, and therefore high gas densities. While temperature-sensitive line ratios change with the metallicity of the gas, they are also strongly affected by the ionization state of the gas. Therefore, shocks and the varying contribution of star formation and AGNs to the ionization become important.

(ii) Table 7 (see column 12) lists objects with  $T_e > 20\,000 \text{ K}$  in each subsample, and we have shown in Section 5.3 that the dusty AGN model grids can fit some of these objects well. Shock heating produces very high temperatures (of the order of millions of K),

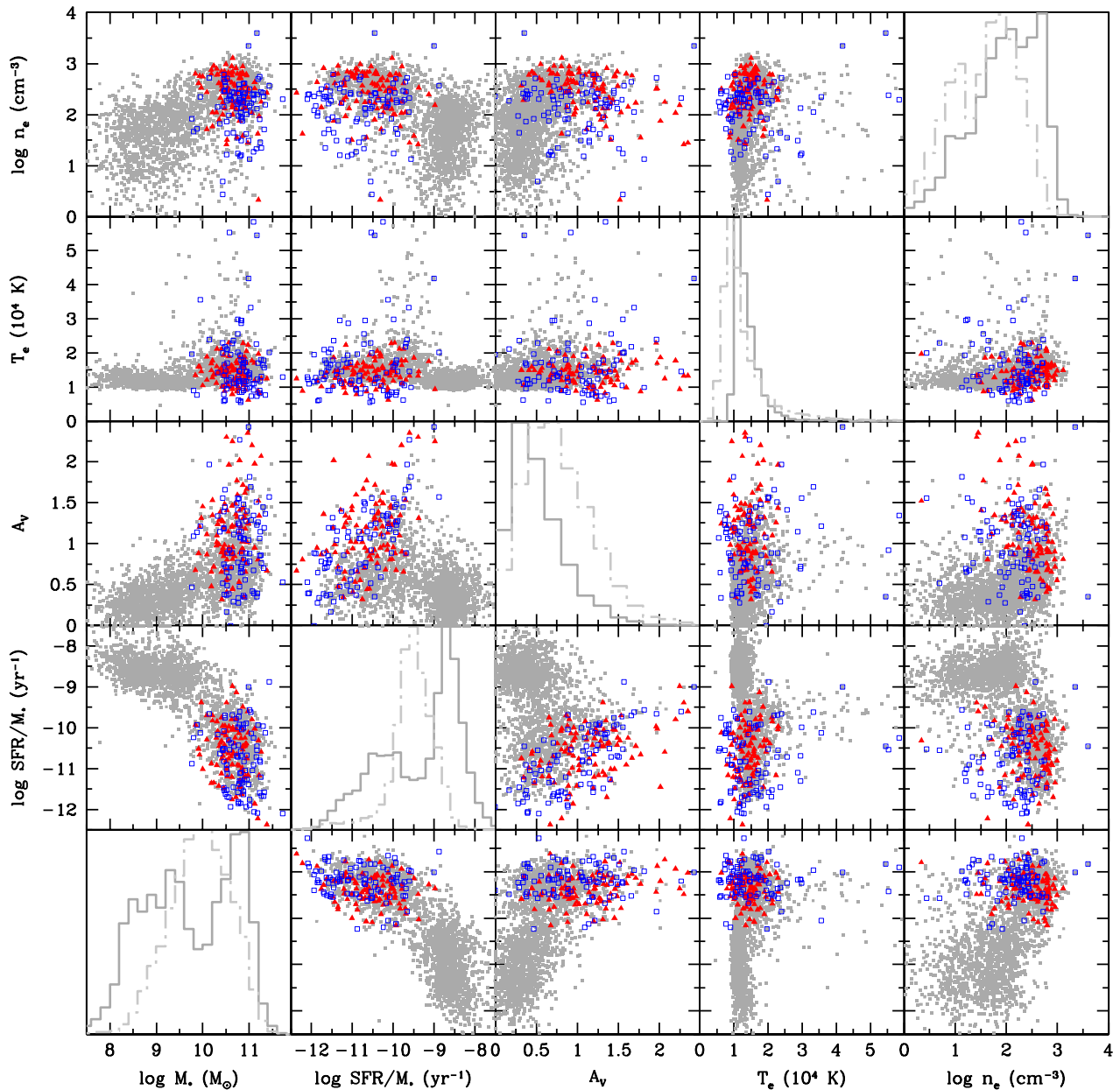


**Figure 11.** Distribution of galaxy properties. The diagonal panels show the normalized distribution of five properties independently:  $M_*$ ,  $\text{SFR}/M_*$ ,  $A_V$ ,  $T_e$  and  $n_e$  (grey solid ones, sample A and sample B; lightgrey dot-dashed histograms, sample C). Objects from samples A and B present a bimodal distribution in  $M_*$ ,  $\text{SFR}/M_*$  is apparent, which is not seen in sample C. The off-diagonal panels show the bivariate distribution of each pair of properties, revealing the complex relationships among them. Red triangles are the NLR-dominated objects, blue open boxes mark out LINERs, while grey dots present objects from samples A and B.

leading to collisional ionization, and the production of highly ionized species. In fact, as we can see from Table 7 and Fig. 11, high  $T_e$  species are more easily found in LINERs and composites with strong [O III]  $\lambda 4363$  emission with certain  $\text{SFR}/M_*$  values. Thus, this indicates high-energy processes in their emission-line regions and the significant contribution of shocks evoked by the active nucleus, and even hot post-asymptotic giant branch stars and white dwarfs must be important (e.g. Stasińska et al. 2008).

Groves, Dopita & Sutherland (2006a) have reported that the observed NLR spectra reveal much flatter mid-IR spectral slopes than those obtained in most NLR models. This suggests that shocks are a possible explanation for the difference between the model and

observed slope. We confirm that it is both sensible and necessary to consider the combination of photoionization and shock. Additional multi-wavelength (especially infrared) observations could be very helpful in achieving this goal.

## 7.2 Strong [O III] narrow-line AGN: low-metallicity candidates?

The physics of the NLR is simpler than that of the broad-line region. The physical conditions are, in fact, similar to H II regions, so that many of the metallicity-sensitive emission line ratios that are routinely applied to star-forming galaxies are also good diagnos-

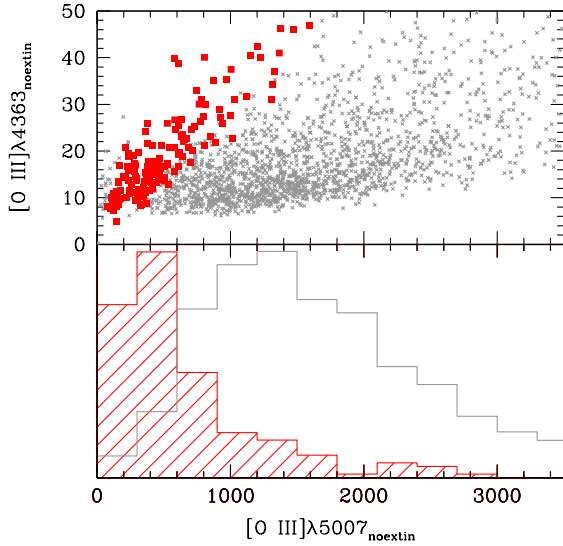


**Figure 12.** *Top:* [O III]  $\lambda 5007$  versus [O III]  $\lambda 4363$  (pre-extinction) correction fluxes in units of  $10^{-17}$  erg/s/cm $^2$ . Red squares are objects with  $T_e > 2 \times 10^4$  K and grey crosses present those with lower  $T_e$ . *Bottom:* normalized histograms of [O III]  $\lambda 5007$  fluxes for the above two groups. Note that only objects from samples A and B are plotted.

tics in the NLRs. Storchi-Bergmann et al. (1998) have calibrated several of these emission line ratios for nearby AGNs, using H II region determined metallicities and photoionization models. However, the similarities between the NLRs and the H II regions in a galaxy lead to ambiguities when estimating abundances. Unless spatially resolved observations can be obtained, it is often difficult to disentangle the contributions to the emission-line spectrum from the NLR and star-forming regions within the galaxy.

Low-metallicity AGNs appear to be very rare objects, at least locally. Currently, emission-line-based estimates of AGN metallicities at both high and low redshifts indicate that AGNs have predominantly solar-to-supersolar metallicities. This phenomenon is expected only if AGNs are old galaxies, are experiencing more supernova explosion events or even mergers, and are sitting on the later part of galaxy evolutionary sequence. From a theoretical point of view, when the total metallicity of a photoionized nebula decreases, there are several effects that cause changes in the final emission-line spectrum (e.g. Dopita & Sutherland 2003; Osterbrock & Ferland 2006). For example, as metallicity decreases, the temperature of the nebula conversely increases. This is a result of the decrease in the efficient cooling metal emission lines and the availability of more high-energy photons to ionize the hydrogen (Sutherland & Dopita 2003).

Using the SDSS DR4 data, Groves et al. (2006b) have found 40 low-metallicity AGN candidates selected out of the 23 000 Seyfert 2 galaxies. They expected that these candidates with masses below  $10^{10} M_{\odot}$  could have metallicities approximately half those of typical AGN. Coincidentally, many of the candidates they found show the [O III]  $\lambda 4363$  line in their spectra. They have suggested that the use of a low-mass selection criterion supported by the observations reveals a correlation between mass- and metal-sensitive line ratios, and that the existence of [O III]  $\lambda 4363$  indicates higher gas temperatures in these objects and thus low metallicities. If their results are correct, we suggest that our strong [O III]  $\lambda 4363$  emission AGNs selected from SDSS DR7 similarly contain low-metallicity AGN candidates (as shown Fig. 7). Using our refined

ranges of density and temperature as input parameters for our NLR modelling, which will be the topic of a companion paper, we aim to reproduce the observational evidence and, as a definite challenge, obtain metallicity calibrations for active galaxies in order to further check these candidates.

## 8 SUMMARY

We have presented a statistical study based on spectroscopy of a large-sample from SDSS DR7. Our sample comprises 15 019 objects with a median redshift  $\sim 0.08$  and is divided based on [O III]  $\lambda 4363$  detection quality: 1100 in sample A (i.e.  $S/N > 5$ ), 1411 in sample B (i.e.  $3 < S/N < 5$ ), and 13 212 in sample C (i.e.  $1 < S/N < 3$ ). First, we determined electron density and electron temperature through  $I[S \text{ II}] \lambda 6716 / \lambda 6731$  and  $I[O \text{ III}] \lambda 5007 / \lambda 4363$ , respectively. To focus on the NLRs, we required that  $\text{FWHM}_{\text{Balmer}} > 300 \text{ km s}^{-1}$  and the physical aperture size  $\ln \phi < 1 \text{ kpc}$  to select the NLR-dominated objects within our sample. Then, we analysed a typical range of  $n_e$  and  $T_e$  of these objects and compared them with those of the host galaxies. Furthermore, we have utilized the plasma diagnostic results along with  $M_{\star}$  and  $\text{SFR}/M_{\star}$  to study the relations between these physical properties for four different classes of emission-line galaxies. Our main results are listed as follows.

- (i) The typical range of density in NLRs of AGNs is  $10^{2-3} \text{ cm}^{-3}$ .
- (ii) The typical range of temperatures in NLRs of AGNs is  $1.0\text{--}2.0 \times 10^4 \text{ K}$  for Seyferts; for LINERs and composites, this range could be higher and wider.
- (iii) Transitions of both  $n_e$  and  $T_e$  from the NLRs to the discs are revealed (i.e. both  $n_e$  and  $T_e$  decrease outwards).
- (iv) Two sequences are proposed:  $T_{\text{LINER}} \gtrsim T_{\text{composite}} > T_{\text{Seyfert}} > T_{\text{star-forming}}$  and  $n_{\text{LINER}} \gtrsim n_{\text{Seyfert}} > n_{\text{composite}} > n_{\text{star-forming}}$ .
- (v) The median value of  $n_e$  is  $\sim 150 \text{ cm}^{-3}$  higher in both Seyferts and LINERs with strong [O III]  $\lambda 4363$  emission than in those with weak [O III] emission, most likely indicating some effect of shocks.
- (vi) LINERs and composites show the median  $T_e$  to be approximately  $2.0 \times 10^4 \text{ K}$ , which is twice as much as that of star-forming galaxies and far too high to be explained by only stellar photoionization.
- (vii) Some strong [O III]  $\lambda 4363$  emission Seyfert 2 galaxies with  $T_e > 15 000 \text{ K}$  can be fitted with dusty AGN model grids at low-metallicity (i.e.  $Z/Z_{\odot} \sim 1$ ).
- (viii) LINERs with strong [O III]  $\lambda 4363$  emission simultaneously contain more dust and indicate the coexistence of old stellar populations and some specific high-energy process.
- (ix) Objects with high  $A_V$  reside in a certain region of the  $M_{\star}$  versus  $\text{SFR}/M_{\star}$  diagram, suggesting that some wide-reaching mechanisms blow out or consume a significant fraction of dust contents, and meanwhile lower  $\text{SFR}/M_{\star}$  for the massive galaxies.
- (x) Considering characteristic present-day star-formation time-scale  $Y$ , we suggest the following relationship:  $Y_L \gtrsim Y_{SY} > Y_C > Y_{SF}$ .
- (xi) Seyferts with strong [O III]  $\lambda 4363$  emissions lie in the high  $M_{\star}$  region and distribute uniformly with those showing weaker [O III]  $\lambda 4363$  emissions (the so-called evolutionary pattern of AGN with high ionization potential). The central nucleus might be responsible for the high ionization potential in Seyferts.
- (xii) The NLR-dominated objects have higher  $M_{\star}$  and lower  $\text{SFR}/M_{\star}$  than the host galaxies, most likely suggesting that the NLRs reside in old and massive active galaxies.

In conclusion, we find several pieces of evidence pointing to additional source(s) of ionization other than the fact that photoionization by hot stars must be working to produce the highly ionized species such as the strong [O III]  $\lambda$ 4363 line in NLRs of AGNs. Previous observations have shown correlations between jets and NLRs. The high gas temperatures and velocity dispersions present in our sample imply that the combination of shock and radiation heating might work as well. The best-known choice of ionization source is the energetic central nucleus, and (weak) shocks might be generated by feedback from AGNs in mergers or by the inflation of cavities by the central AGN. With our refined ranges of density and temperature as input parameters for the AGN NLR modelling, in a companion paper, we intend to reproduce the observational spectra and, furthermore, to obtain metallicity calibrations for active galaxies.

#### ACKNOWLEDGMENTS

Zhitai Zhang dedicates her first research paper in astronomy to Professor Dame Jocelyn Bell Burnell who has played a leading role in our great understanding of the Universe. Her legend gives young minds a compass beyond the reach of science.

Zhitai Zhang especially expresses her sincere thankfulness to Professor Gang Zhao (NAOC) for his gentle guidance.

We gratefully acknowledge the anonymous referee for a careful and constructive revision that has improved this manuscript. The authors especially thank Jarle Brinchmann (Leiden University) for providing a number of detailed and crucial comments and suggestions, which have significantly enhanced this work. We also thank C. R. O'Dell (Vanderbilt University) and X. W. Liu (KIAA-PKU) for inspired pre-research discussions relating to the understanding of nebulae ionization structures, and L. Hao (SHAO) for sharing some interesting thoughts on the SDSS data.

Funding for the creation and distribution of the SDSS-I and SDSS-II Archive has been provided by the Alfred P. Sloan Foundation, the Participating Institutions, the National Aeronautics and Space Administration, the National Science Foundation, the US Department of Energy, the Japanese Monbukagakusho and the Max Planck Society. The SDSS web site is <http://www.sdss.org>. Data products of SDSS DR7 have been publicly released by MPA/JHU group, a collaboration of researchers (current or former) from the MPA and the JHU, who have made their measured quantities on SDSS galaxies publicly available. This work was supported by the Natural Science Foundation of China (Grant Nos. 10933001 and 11273026).

#### REFERENCES

- Abazajian K. et al., 2009, *ApJ*, 182, 543  
 Adelman-McCarthy J. et al., 2008, *ApJS*, 175, 297  
 Aird J. et al., 2012, *ApJ*, 746, 90  
 Allen M.G., Groves B.A., Dopita M.A., Sutherland R.S., Kewley L.J., 2008, *ApJS*, 178, 20  
 Baldwin J.A., Phillips M.M., Terlevich R., 1981, *PASP*, 93, 5 (BPT)  
 Barth A.J., Ho L.C., Filippenko A.V., Rix H.W., Sargent W.L.W., *ApJ*, 546, 205  
 Baskin A., Laor A., 2005, *MNRAS*, 358, 1043  
 Bennert N., Falcke H., Shchekinov Y., Wills B.J., 2002, *ApJ*, 574, L105  
 Bennert N., Jungwiert B., Komossa S., Haas M., Chini R., 2006, *A&A*, 456, 953  
 Binette L., Wilson A.S., Storchi-Bergmann T., 1996, *A&A*, 312, 365  
 Brinchmann J., Charlot S., White S.D.M., Tremonti C.A., Kauffmann G., Heckman T., Brinkmann J., 2004, *MNRAS*, 351, 1151  
 Charlot S., Kauffmann G., Longhetti M., Tresse L., White S.D.M., Maddox S.J., Fall S.M., 2002, *MNRAS*, 330, 876  
 Clarke C., Oey M.S., 2002, *MNRAS*, 337, 1299  
 Collins N.R., Kraemer S.B., Crenshaw D.M., Bruhweiler F.C., Meléndez M., 2009, *ApJ*, 694, 765  
 de Robertis M.M., Dufour R.J., Hunt R.W., 1987, *JRASC*, 81, 195  
 Dopita M.A., Sutherland R.S., 2003, *Astrophysics of the Diffuse Universe* (Berlin: Springer)  
 Dopita M.A., Groves B., Sutherland R.S., 1995, *ApJ*, 455, 468  
 Dopita M.A., Groves B., Sutherland R.S., 1996, *ApJ*, 102, 161  
 Ferland G.J., Netzer H., 1983, *ApJ*, 264, 105  
 Fitzpatrick E.L., 1999, *PASP*, 111, 63  
 Gallazzi A., Charlot S., Brinchmann J., White S.D.M., Tremonti C.A., 2005, *MNRAS*, 362, 41  
 Groves B.A., 2007, *The Central Engine of Active Galactic Nuclei ASP Conference Series*, Vol. 373  
 Groves B., Allen M.G., 2010, *NewA*, 15, 614  
 Groves B., Dopita M., Sutherland R., 2004a, *ApJS*, 153, 9  
 Groves B., Dopita M., Sutherland R., 2004b, *ApJS*, 153, 75  
 Groves B., Dopita M., Sutherland R., 2006, *A&A*, 458, 405  
 Groves B.A., Heckman T.M., Kauffmann G., 2006, *MNRAS*, 371, 1559  
 Groves B., Brinchmann J., Walcher C.J., 2012, *MNRAS*, 419, 1402  
 Hao L. et al., 2005, *ApJ*, 129, 1783  
 Hao L. et al., 2005, *ApJ*, 129, 1795  
 Heavens A., Panter B., Jimenez R., Dunlop J., 2004, *Nature*, 428, 625  
 Heckman T.M., Balick B., 1979, *A&A*, 79, 350  
 Heckman T.M., Miley G.K., van Breugel W.J.M., Butcher H R., 1981, *ApJ*, 2247, 403  
 Ho L.C., 1996, *The Physics of LINERs in View of Recent Observations*, San Francisco: ASP, p.103  
 Ho L.C., 2008, *ARA&A*, 46, 475  
 Hogg D.W., Finkbeiner D.P., Schlegel D.J., Gunn J.E., 2001, *AJ*, 122, 2129  
 Hopkins P.F., Cox T.J., Younoer J.D., Hernquist L., 2009, *ApJ*, 691, 1168  
 Ivezić Z., 2004, *Astron. Nachr.*, 325, 583  
 Kalsner M.E., et al., 2000, *ApJ*, 528, 260  
 Kauffmann G. et al., 2003a, *MNRAS*, 341, 33  
 Kauffmann G. et al., 2003b, *MNRAS*, 341, 54  
 Kauffmann G. et al., 2003c, *MNRAS*, 346, 1055 (Ka03)  
 Kauffmann G., White S.D.M., Heckman T., Ménard B., Brinchmann J., Charlot S., Tremonti C.A., Brinkmann J., 2004, *MNRAS*, 353, 713  
 Kewley L.J., Dopita M.A., Sutherland R.S., Heisler C.A., Trevea J., 2001, *ApJ*, 556, 121 (Ke01)  
 Kewley L.J., Jansen R.A., Geller M.J., 2005, *PASP*, 117, 227  
 Kewley L.J., Groves B., Kauffmann G., Heckman T., 2006, *MNRAS*, 372, 961 (Ke06)  
 Kollatschny W., Wang T.G., 2008, *Ap&SS*, 303, 123  
 Komossa S., Schulz H., 1997, *A&A*, 323, 31  
 Koski A.T., 1978, *ApJ*, 223, 56  
 Kraemer S.B., Ruiz J.R., Crenshaw D.M., 1998, *ApJ*, 508, 232  
 Kraemer S.B., Trippe M.L., Crenshaw D.M., Meléndez m., Schmitt H.R., Fischer T.c., 2009, *ApJ*, 698, 106  
 Liu X., Shen Y., Strauss M.A., Greene J.E., 2010, *ApJ*, 708, 427  
 Lupton R.H. et al., 2001, in Hamden F. R., Jr, Primini F. A., Payne H. E., eds, *ASP Conf. Ser. Vol. 238, Astronomical Data Analysis Software and Systems X. Astron. Soc. Pac., San Francisco*, p. 269  
 Nagao T., Murayama T., Taniguchi Y., *ApJ*, 549, 155  
 Netzer H. et al., 2004, *ApJ*, 641, 558  
 O'Donnell J.E., 1994, *ApJ*, 422, 158  
 Osterbrock D.E., 1983, *PASP*, 95, 12  
 Osterbrock D.E., de Robertis M.M., 1985, *PASP*, 97, 1129  
 Osterbrock D.E., Ferland G., 2006, *Astrophysics of Gaseous Nebulae and Active Galactic Nuclei*. -2nd ed. University Science Books, Mill Valley, CA  
 Osterbrock D.E., Miller J.S., 1975, *ApJ*, 197, 535



- Pier J.R., Jeffrey R., Munn J.A., Hindsley R.B., Hennessy G.S., Kent S.M., Lupton R.H., Ivezić Z., 2003, *AJ*, 125, 1559
- Rodríguez-Ardila A., Pastoriza M.G., Donzelli C.J., 2000, *ApJS*, 126, 63
- Salim S. et al., 2007, *ApJS*, 173, 267
- Schaerer D., de Barros S., Sklias P., 2012, *A&A*, 549, A4
- Shaw R.A., Dufour R.J., 1995, *PASP*, 107, 896
- Shen Y., Liu X., Greene J.E., Strauss M.A., 2011, *ApJ*, 735, 48
- Smith J.A. et al., 2002, *AJ*, 123, 2121
- Stasińska G., Vale Asari N., Cid Fernandes R., Gomes J.M., Schlickmann M., Mateus A., Schoenell W., Sodr e L., Jr, 2008, *MNRAS*, 391, L29
- Storchi-Bergmann T., Schmitt H.R., Calzetti D., Kinney A.L., 1998, *AJ*, 115, 909
- Stoughton C. et al., 2002, *AJ*, 123, 485
- Sulentic J.W., Marziani P., Dultzin-Hacyan D., 2000, *ARA&A*, 38, 521
- Sutherland R.S., Dopita M.A., 1993, *ApJS*, 88, 253
- Tremonti C.A. et al., 2004, *ApJ*, 613, 898
- Tucker D.L. et al., 2006, *Astron. Nachr.*, 327, 821
- Vaona L., Ciroi S., Di Mille F., Cracco V., La Mura G., Rafanelli P., 2012, *MNRAS*, 427, 1266
- Veilleux S., Osterbrock D.E., 1987, *ApJ*, 63, 295
- Walsh J.R., 1983, *A&A*, 123, 101
- Xu D.W., Komossa S., Zhou H.Y., Wang T.G., Wei J.Y., 2007, *ApJ*, 670, 60
- York D.G. et al., 2000, *AJ*, 120, 1579
- Zhou H., et al., 2006, *ApJSS*, 166, 128

This paper has been typeset from a  $\text{T}_{\text{E}}\text{X}/\text{L}^{\text{A}}\text{T}_{\text{E}}\text{X}$  file prepared by the author.